Ageing and energy performance analysis of a utility-scale lithium-ion battery for power grid applications through a data-driven empirical modelling approach

Journal of Energy Storage 65 (2023) 107232

Contents lists available at ScienceDirect

Journal of Energy Storage

journal homepage: www.elsevier.com/locate/est

Research papers

Ageing and energy performance analysis of a utility-scale lithium-ion battery for power grid applications through a data-driven empirical modelling approach

Alberto Grimaldi [a,b,*], Francesco Demetrio Minuto [a,b], Alessandro Perol [c], Silvia Casagrande [c], Andrea Lanzini [a,b]

[a] Department of Energy, Politecnico di Torino, Corso Duca degli Abruzzi 24, 10129 Torino, Italy
[b] Energy Center Lab, Politecnico di Torino, Via Paolo Borsellino 38/16, 10138 Torino, Italy
[c] Edison S.p.A., Via Paolo Borsellino 38/16, 10138 Torino, Italy

ARTICLE INFO

Keywords:
Li-ion BESS
Grid-connected battery
Stationary application
Battery ageing
Battery storage system efficiency
Power grid applications

ABSTRACT

Energy storage systems are becoming one of the most relevant technologies to effectively support renewable energy source (RES) deployment at large. The present work proposes a detailed ageing and energy analysis based on a data-driven empirical approach of a real utility-scale grid-connected lithium-ion battery energy storage system (LIBESS) for providing power grid services. The system under investigation is an operative utility-scale LIBESS integrated with a multi-MW PV plant and connected to the medium voltage network, located in Southern-Italy. The ageing and energy analysis has been performed using data measured by the supervisory control and data acquisition (SCADA) system directly connected with the LIBESS. This large amount of data is collected in a cloud database and then elaborated using proper software tools. This experimental campaign applied on a commercial LIBESS covers the impact of degradation mechanisms, such as cycle and calendar ageing, the battery and global system efficiency as well as the role of auxiliaries' power consumption under normal and power grid services operations. Thanks to the low complexity of the proposed data-driven model, it could be easily replicated in any other LIBESS facility, both operative in real-world framework and in laboratory context. The state-of-health (*SOH*) estimated by the degradation model implemented in this work after 3 years of operations and after 356 full-cycles equivalents is equal to 95.88 %, with an average capacity loss compared to the nominal capacity of about 1.37 % per year. Energy analysis revealed an average system global efficiency of 85 % for operations close to the nominal power that decreases to 65 % for operations at low power rates. While considering the grid network services operations, the power grid applications investigated are primary frequency regulation, secondary voltage regulation and PV unbalances reduction. Our results show that primary frequency regulation is the most efficient service in terms of ageing and energy performances. It has been evaluated a capacity loss of 0.03 kWh per each full-cycle equivalent performed during primary frequency regulation. Differently, secondary voltage regulation and PV unbalances reduction present a capacity loss of 0.1 kWh and of 0.05 kWh per each full-cycle equivalent, respectively. At the same time, the global efficiency of primary regulation (around 83 %) is remarkably higher compared to secondary voltage regulation (about 47 %) and to PV unbalances reduction (about 55 %). Results support the relevance to identify the most impacting key performance indicators for effective exploitation of LIBESS in power system and network services applications.

1. Introduction

The increasing penetration of renewable energy source (RES) in the national energy mix requires more flexible power distribution networks to manage injections variability. Nowadays stationary utility-scale energy storage systems are an essential element to meet the requirements of the rapid increase of renewable energy sources (RESs) penetration into the power distribution network. Due to recent improvements of technology [1], economy of scale [2], bankability [3], and new regulatory initiatives, the amount of lithium-ion battery energy storage systems (LIBESS) is constantly increasing worldwide. In this

* Corresponding author at: DENERG, Politecnico di Torino, Corso Duca degli Abruzzi 24, 10129 Torino, Italy.
E-mail address: alberto_grimaldi@polito.it (A. Grimaldi).

https://doi.org/10.1016/j.est.2023.107232
Received 16 January 2023; Received in revised form 19 March 2023; Accepted 22 March 2023

Nomenclature

Abbreviations

BESS	battery energy storage system
BMS	battery management system
BOL	beginning-of-life
CB	confidence bounds
DOD	depth of discharge
EMS	energy management system
EOL	end-of-life
EPI	energy performance indicator
ESS	energy storage system
GHG	greenhouse gas
HESS	hybrid energy storage system
HVAC	heating ventilation air conditioning
KPI	key performance indicator
LDES	long duration energy storage
LIBESS	lithium-ion battery energy storage system
NMC	nickel manganese cobalt
PCS	power conversion system
PFR	primary frequency regulation
PGA	power grid application
POD	point of delivery
PUR	PV unbalances reduction
RES	renewable energy sources
RFB	redox flow battery
SOC	state of charge
SOEC	solid-oxide electrolyser
SOFC	solid-oxide fuel cell
SVR	secondary voltage regulation
SCADA	supervisory control and data acquisition
TMS	thermal management system

Ageing parameters

C_0	LIBESS capacity at the beginning of the observation period [%]
C_{deg}^{cyc}	cycle degradation [%]
C_{deg}^{cal}	calendar degradation [%]
C_{deg}	total degradation [%]
C_{deg}^{FCE}	ageing effect factor [kWh/FCE]
ΔDOD	cycle depth of discharge [−]
ΔDOD_{ref}	cycle depth of discharge in reference conditions [−]
$f_{\Delta DOD}^{cyc}$	cycle degradation stress factor model related to ΔDOD [−]
f_{SOC}^{cyc}	cycle degradation stress factor model related to SOC [−]
f_{T}^{cyc}	cycle degradation stress factor model related to T [−]
f_{SOC}^{cal}	calendar degradation stress factor model related to SOC [−]
f_{T}^{cal}	calendar degradation stress factor model related to T [−]
F_{deg}^{cyc}	cycle ageing model for the battery [−]
F_{deg}^{cal}	calendar ageing model for the battery [−]
FCE_0	full-cycles equivalents at the beginning of the observation period [FCE]
FCE	full-cycles equivalents during the observation period [FCE]
$S_{\Delta DOD}^{cyc}$	cycle degradation stress factor coefficient related to ΔDOD [−]
S_{SOC}^{cyc}	cycle degradation stress factor coefficient related to SOC [−]
S_{T}^{cyc}	cycle degradation stress factor coefficient related to T [−]
S_{SOC}^{cal}	calendar degradation stress factor coefficient related to SOC [−]
S_{T}^{cal}	calendar degradation stress factor coefficient related to T [−]
SOC_{ref}	average state of charge in reference conditions [%]
$SOC_{avg,cyc}$	average state of charge during cycling [%]
$SOC_{avg,cal}$	average state of charge during storage [%]
SOH	state of health [%]
t_0	calendar age of the battery at the beginning of the observation period [s]
t	time period for which the calendar ageing is estimated [s]
T	battery temperature [°C]
T_{ref}	battery temperature in reference conditions [°C]

Energy parameters

$C\text{-}rate$	charge/discharge rate [C]
dt	sampling rate [s]
DOD_{max}	maximum depth of discharge [−]
$E_{available}$	available capacity [kWh]
E_{actual}^{bat}	actual capacity [kWh]
E_{nom}^{bat}	nominal capacity [kWh]
$E_{AC,dh}$	AC discharged energy [kWh]
$E_{AC,ch}$	AC charged energy [kWh]
E_{AUX}	energy consumed by auxiliaries [kWh]
η_{AC}	AC round-trip efficiency [−]
η_{global}	global efficiency [−]
L_{global}	share of global losses [−]
L_{AUX}	share of auxiliaries losses [−]
P_{AC}	AC power [kW]
P_{nom}	nominal LIBESS power [kW]
P	AC power normalized [p.u.]
P_{AUX}	auxiliary mean power [kW]
$P_{AUX,nom}$	nominal power of the LIBESS auxiliaries [kW]
P_{AUX}^{norm}	auxiliary mean power normalized [p.u.]
R^2	coefficient of determination (R-squared) [−]
SSE	sum of squared error [−]
SSR	sum of squared regression [−]
SST	sum of squared total [−]
SOC_{min}	lower bound of SOC [%]
SOC_{max}	upper bound of SOC [%]
T_{amb}	ambient temperature [°C]
T_{PFR}	average LIBESS racks temperature during PFR [°C]
T_{PUR}	average LIBESS racks temperature during PUR [°C]
T_{SVR}	average LIBESS racks temperature during SVR [°C]

perspective, there is a growing body of literature that recognises the importance in modelling the operation of utility-scale battery energy storage systems for power grid applications [4].

As reported by IEA World Energy Outlook 2022 [5], installed battery storage capacity, including both utility-scale and behind-the-meter, will have to increase from 27 GW at the end of 2021 to over 780 GW by 2030 and to over 3500 GW by 2050 worldwide, to reach net-zero emissions targets. It is expected that stationary energy storage in operation will reach about 1095 GW/2850 GWh, mostly in electrochemical batteries forms [6]. Specifically, deployments of grid-connected LIBESS are projected to increase considerably from 1.5 GW in 2020 to 8.5 GW in 2030 [7]. From an economic point of view, the capital cost of utility-scale stationary batteries will have to decrease from 310 USD/kWh in 2020 to 130 USD/kWh by 2050 [5]. Worldwide, the global revenue was around USD 220 million in 2014 and is expected to increase to USD 18 billion in 2023 [8]. At EU level, European battery sales for utility-scale applications will grow from USD 56 million in 2014 to USD 5 billion until 2023 [8].

While the integration of RESs into power grids is offering great benefits in terms of greenhouse gases (GHGs) mitigation, energy access and energy security, these inexhaustible sources are characterized by fluctuating power output. Due to their intermittent nature, high RESs penetration may put power systems stability at risk, causing grid frequency and voltage fluctuations. In fact, the growing RES penetration and the simultaneous reduction of conventional thermoelectric plants generates a reduction of the inertia of the electrical system, which is essential to guarantee the frequency stability and the ability to withstand network perturbations. As a result, an evolution of the electric system is fundamental. This evolution consists of passing from large conventional generation plants to a more flexible electric system composed by large/medium generation plants plus consumers' resources (demand response), distributed generation, renewables and storage systems.

In recent years, the topic about the evolution of the electrical system has gained an increasing interest in the energy sector. At EU level, the Clean Energy Package [9] and the European Green Deal [10] define a new set of rules aimed to update the European energy policy framework to facilitate the transition from fossil fuels towards cleaner energy sources. Concerning GHGs emissions targets, currently EU has reached a reduction of 23 % with respect to the year 1990 considered as the baseline-year. In 2030 this reduction must increase up to 55 % and in 2050 the target is to achieve net zero emissions. To reach these targets the key action is to increase the RES penetration in the European energy mix up to 80–90 % within 2050 [10]. Therefore, it will be necessary to adapt the power distribution grid due to the progressive RES penetration, making it more flexible and improving the interconnections and digitalization. To support the electrification and RES penetration, energy storage systems such as batteries are fundamental. All these actions are monetary supported by European Union and as reported in the Green New Deal [10], at least 1 trillion Euros will be used for sustainable investments over the next 10 years.

Consequently, an increasing number of stakeholders and policy makers from industry and research fields are focused on simulating the BESS operation. A.V. Vykhodtsev et al. [11] have developed a detailed overview about modelling approaches to characterize LIBESS in techno-economic analysis of power systems. The aim of this review is to help modellers to select an appropriate battery model that fits their needs in LIBESS energy management. The LIBESS models can be divided into black-box, phenomenological, and physical models [12]. The battery is typically modelled from two extreme viewpoints: the cell level and the system level. The former is focused on the precise characterization of the operation of a single lithium-ion cell, while the latter considers the LIBESS as a single unit that can store and release energy following the operator instructions. A real BESS is composed by a set of lithium-ion cells, the power conversion system (PCS), the battery management system (BMS), and the thermal management system [13]. Despite the importance of all these units during BESS operation, it is worthwhile to point out that in literature most of the studies are mainly focused on the electrochemical section of a BESS, hence a lack is recognized in the modelling of the overall BESS performances. Beside the electrochemical section, the other units of a BESS are the power conversion system (PCS) and other devices providing auxiliary services (e.g., heating ventilation air conditioning HVAC system, SCADA, control and monitoring system, alarms, motorized switches, lightening). Despite these loads are not negligible when evaluating the losses in operation, there have been few empirical investigations about the role of auxiliaries' consumption during BESS operation [14]. During BESS lifetime it is crucial to manage properly HVAC system settings, to reduce the capacity fade due to cycling and calendar ageing [15].

Another peculiar aspect that only few researchers added to the battery model is evaluating the impact of the thermal and conversion systems on the decision-making process. M. Schimpe et al. [13] have conducted a detailed energy efficiency evaluation of a stationary lithium-ion battery container system via electro-thermal modelling. They offered a holistic approach to calculate conversion losses and auxiliaries' power consumption by identifying up to 18 energy loss mechanisms. Several grid applications were simulated for estimation of real-world performance. A remarkable amount of literature has been published on electrochemical cells modelling [11,16]. Generally, experimental campaigns are significantly expensive due to required measurements campaign in specialized laboratories. Brivio et al. [17] have been proposed new laboratory protocols to simplify the measurement process, leading to a standard quantification of the cells' performance.

The existing research is primarily focused on the cell-level point of view, without considering the entire BESS units. In fact, in most real-life BESS analysis, the plant manager cannot perform laboratory tests on a single cell [18]. Moreover, the cell performance is strongly influenced by BMS and PCS settings and control rules. A large amount of LIBESS numerical models with different degrees of complexity can be found in literature, especially applied on a single cell, and then extended to the complete BESS, by assuming that all cells behave equally. However, it is crucial to extrapolate actual system performance based on different operating conditions to derive a battery system model that can be suitable in evaluating the most impactful KPIs of the grid services provided by a battery energy storage system. This study overcomes this gap by developing a data-driven model for battery performance and ageing based on real data provided by a LIBESS currently in operation. Rancilio et al. [18] have suggested an experimental BESS model design for the analysis of power grid applications, developing a BESS model on laboratory-scale tests. In this paper we adopt the methodology presented in [18] to analyse a full-scale LIBESS data.

Several researchers have proposed a literature survey on battery grid applications. D. Choi et al. [19] have proposed a comprehensive overview of the current status and challenges of Li-ion BESS for grid applications, giving information about the time scale of each service based on real-world projects. In [11] a detailed literature survey on battery grid applications has been proposed, focusing on battery modelling approaches, degradation description, and optimization techniques adopted. In [13] the energy performance of a stationary LIBEES has been evaluated during the provision of primary control reserve, secondary control reserve and the storage of surplus photovoltaic. Importantly, in [18] the automatic frequency restoration reserve network service has been simulated evaluating the most impacting KPIs. Xu et al. [20] proposed an optimal control and bidding policy of battery participation in frequency regulation markets, also considering the cost of battery ageing in operating strategies to maximize market profits. Similarly, in [21] a multiscale linear programming formulation has been applied to evaluate the storage system degradation for both energy and ancillary services in day-ahead and real time market.

Cycle-life degradation analysis requires the determination of the number of full-cycles performed by a BESS in a specific period of time. The main difficulty in cycle counting for BESS operations is the presence of incomplete charge/discharge cycles characterized by variable depth of discharge (DOD) values. As the cycle-life degradation changes for different DOD ranges, all the micro-cycles (small amplitude cycles within a main charge/discharge time series) present in a DOD profile over a selected observation period needs to be accounted to evaluate the total number of full-cycles equivalents and therefore the total degradation occurring during the BESS cycle-life. The "Rainflow Counting" method, developed by Matsuishi and Endo in 1968 [22] for metal fatigue analysis, is used to identify individual cycles in a given time span. Due to the similarity of irregular stress cycles for metal components with the irregular DOD cycles for a battery, this counting algorithm gained interest for BESS life degradation analysis [23]. Concerning the applications on grid network services, authors in [24] have applied Rainflow Counting algorithm to estimate BESS life degradation caused by providing frequency regulation ancillary services. H. Rauf et al. [25] have conducted a detailed review on the studies that have been published for state-of-health (*SOH*) estimation in the last 10 years,

confirming that *SOH* is a crucial parameter to model Li-ion battery's degradation. In the literature, degradation models are typically incorporated into BESS models, especially during network services provision. He et al. [26] have developed a battery cycle life model incorporated into a profit maximization model, to determine the optimal bids in day-ahead energy, spinning reserve, and regulation markets. In [27] a novel degradation cost model based on depth of discharge and discharge rate has been adopted on a BESS participating in energy, ancillary services, and capacity markets. Hesse et al. [28] have elaborated an optimal dispatch strategy for storage systems trading on energy arbitrage markets. They emphasize the relevance of considering both ageing and energy conversion losses in battery system dispatch optimisation. Battery ageing could be described as a composition of two degradation mechanisms: cycle and calendar ageing. Ageing under operational load is defined as cycle ageing, whereas ageing without load is defined as calendar ageing. Therefore, cycle ageing occurs when batteries are actively dispatched at non-zero power. On the other hand, calendar ageing accounts of all degradation processes that results independent of dispatch and occurs when the batteries at rest [29]. In this work, the total degradation is evaluated as the sum of the cycle and calendar ageing of the battery, which are assumed to be independent of each other. This independence assumption is widely applied on the existing literature [30–33]. However, as proposed by Raj et al. [34], degradation may be sensitive to their order and periodicity – a phenomenon that has been called "path independence". Since this work is focused on the degradation resulting from participation in grid applications, and not on chemical phenomena occurring inside the battery cells, the cycle and calendar ageing are treated separately, and their contribution is added together to form a combined model.

Concerning the context of data-driven modelling, it is crucial to analyse and reprocess the raw data before any modelling task, in order to address data inconsistency and noise issues and achieve effective models [35]. The measurement noises are a key factor affecting the performance of battery models and battery state estimation approaches, and larger measurement noise will inevitably degrade the model accuracy affecting the state estimation results [36]. To better account the noise influence on the model parameters, Lucu et al. [37] have been developed a data-driven ageing model for Li-ion batteries under the Gaussian Process framework. They have been emphasized the relevance of using the Gaussian Process model to learn from new data observations, providing more accurate and confident predictions. Similarly, Li et al. [38] built a bias compensation recursive least square (LST) denoising method to improve the online model identification and SOC estimation method. Additionally, Wei et al. [39], proposed a Frisch scheme-based bias compensation RLS to compensate the noise effect. The data used in this work for the empirical model is gathered from the BMS of the battery, which is designed to pre-process and filter out any noise or inconsistency in the measurements. Therefore, we did not perform noise analysis as we assume the data provided for our modelling task is already accurate and reliable. However, we conducted a large set of experiments, which have been repeated multiple times to ensure the consistency and reliability of the results.

The novelty of our paper is to consider a real-world BESS currently in operation. This operative utility-scale PV-integrated LIBESS is analysed in terms of ageing and energy performance. Precise ageing key performance indicators (KPIs) and energy performance indicators (EPIs) were evaluated by performing specific experimental tests on the LIBESS currently in operation. The aim of this study is to develop a data-driven numerical model suitable for analysing different power grid applications. In our data-driven model, real charge/discharge working cycles performed by the LIBESS are elaborated. The grid services investigated in this work are primary frequency regulation (PFR), secondary voltage regulation (SVR) and PV unbalances reduction (PUR). As a result, the identification of the most impacting KPIs and EPIs may help power plant managers to properly simulate different layouts of grid services.

The remainder of the paper is organised as follows. In Section 2 a description is given for the LIBESS layout under investigation and for the data acquisition system. In Section 3 it is presented the methodology implemented to build the data-driven empirical model. Section 4 is focused on results. Particularly, the ageing analysis is applied considering different observation periods, while the energy efficiency and auxiliary energy consumptions are evaluated as a function of the AC battery power, thus obtaining empirical mathematical correlations. Finally, Section 5 includes conclusions and foreseen next steps.

2. Experimental set-up

2.1. LIBESS layout

The BESS under investigation is a Li-Ion BESS for stationary applications currently in operation, located in Southern-Italy. The container storage system is composed by the lithium-ion BESS and by other peripheral auxiliaries' components such as the energy management system (EMS) and the thermal management system (TMS). The bi-directional inverter is responsible for converting the DC power flows into AC power flows and vice versa. According to the sign convention, the power flows are considered positive during the discharge mode, while negative during the charge mode. The AC power flows are exchanged through the grid interface. The battery is integrated with a MW-scale PV plant and can provide power grid services. In Fig. 1 a simplified version of the LIBESS layout is represented.

The LIBESS is composed by two Li-ion nickel-manganese-cobalt (NMC) battery packs, with an overall nominal power (P_{nom}) of 500 kW and a nominal energy (E^{bat}_{nom}) of 822 kWh. Each battery pack contains 9 modules, clustered in 6 racks via parallel connection. Each module is composed by 22 cells connected in series. The NMC cells operate in the voltage range between $2.5 - 4.23\ V$, corresponding to a maximum energy content at C/3 rate of 346 Wh. Inside this voltage range, the manufacturer has defined the available operative field, comprised between $SOC_{min} = 10\%$ and $SOC_{max} = 90\%$, to avoid under-discharge and over-charge operations, respectively. Consequently, the available capacity is equal to the product between the nominal capacity and the maximum depth of discharge, as expressed by Eq. (1):

$$E_{available} = E^{bat}_{nom} \cdot DOD_{max} = 822 \cdot 0.8 = 657.6\ [kWh] \tag{1}$$

2.2. Data acquisition system

The operations of the LIBESS were supervised via the local supervisory control and data acquisition (SCADA) system installed inside the battery storage container. Data are continuously measured and recorded with 1 s sampling rate. The measurements are collected in a cloud database. One of the advantages of collecting high-resolution data is the possibility to easily change the sampling rate from 1 s to larger sampling rates. The variables measured by the SCADA and then elaborated are listed as follows, with their native sampling rates:

- State of charge (SOC) values with 1 s sampling rate.
- DC parameters, such as voltage, current, charged/discharged battery power with 1 s sampling rate.
- AC parameters, like AC charged/discharged battery power, AC power exchanged at point of delivery (POD), auxiliaries' power consumption with 1 s sampling rate.
- Average racks temperatures and container zones temperatures with 60 s sampling rate.

These parameters, extracted during the selected observation periods, are used as input for the data-driven ageing and energy model described in the next section.

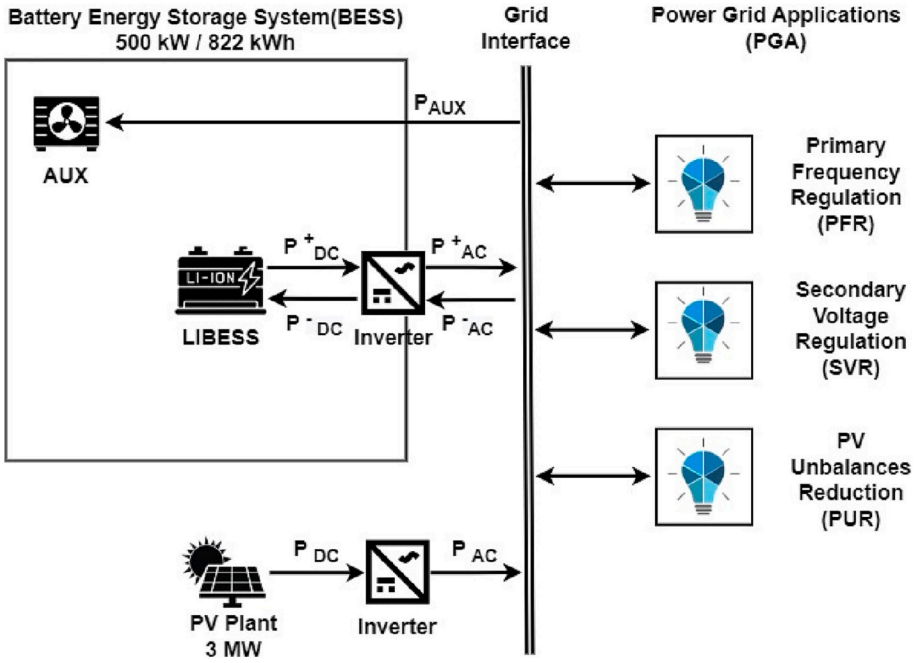

Fig. 1. Utility-scale grid-connected LIBESS layout.

3. Methodology

This section provides an overview of the data analysis methodology implemented in this work. Firstly, the ageing analysis based on a specific semi-empirical model is applied over different observation periods. Secondly, the energy performance analysis is focused on finding an empirical correlation between the AC round-trip efficiency and the discharged/charged power using the battery. Similarly, the role of auxiliaries' consumption is investigated for different power rates and for different power grid applications.

3.1. Ageing analysis

The ageing analysis is aimed to evaluate the state-of-health (*SOH*) of the LIBESS under investigation. *SOH* is defined as the status of battery health to supply power and energy compared to its capability at the initial state [25]. Its mathematical definition is expressed as the ratio of the actual capacity E^{bat}_{actual} with respect to the nominal capacity of the battery E^{bat}_{nom} (Eq. (2)):

$$SOH = \left(E^{bat}_{actual}/E^{bat}_{nom}\right)\cdot 100\ [\%] \tag{2}$$

The SOH indicator is used to determine the need for battery replacement. Typically, the end-of-life (EOL) condition of a battery is reached when the actual battery capacity degrades to 80 % of original capacity, corresponding to 20 % of capacity loss [33].

The ageing degradation model presented in this work was developed according to the operating principle illustrated in Fig. 2. It estimates the capacity degradation of the battery occurring during the observation period as the loss of energy (measured in terms of lower actual capacity) compared to the nominal capacity. This model is composed by two main parts: cycle degradation model and calendar degradation model. The final output is the total degradation calculated as the sum of the outputs of these two sub-models.

Typically, to quantify ageing during operational and no operational load conditions, the stress factors cycle depth of discharge, average state of charge during cycling and during storage, average battery temperature and time of storage can be used [40,41]. Empirical BESS ageing models are implemented to quantify the individual influence of the stress factors in dependence of charge-throughput during cycle ageing and time during calendar ageing. These BESS ageing models are based on algebraic expressions for capacity fade that are empirically parametrized on experimental ageing tests [42,43]. Collath et al. [44] have developed a complete review about relevant ageing mechanisms, ageing stress factors, and degradation models for BESS operations. Accordingly,

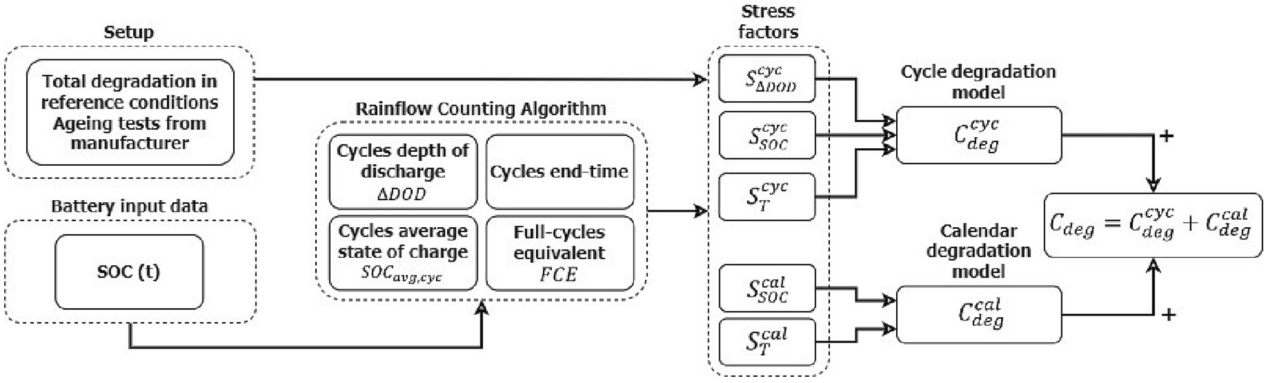

Fig. 2. The operating principle of the ageing degradation model.

in this work, empirical algebraic equations are used to estimate the cycle and calendar ageing.

The cycle degradation model evaluates the capacity degradation occurring due to operation of the battery. This capacity degradation depends on the four degradation stress factors related to cycle ageing: cycle depth of discharge (ΔDOD), average state of charge during cycling ($SOC_{avg,cyc}$), average battery temperature (T) and the number of cycles cycled during the observation period, expressed in full-cycles equivalents (FCE). Cycle depths of discharge, average state of charge of the cycles and number of full cycles are determined from the SOC time series data applying the Rainflow Counting algorithm [22].

The calendar degradation model calculates the capacity degradation caused by degradation processes not related to charge-discharge cycling. This evaluation is based on the three degradation stress factors responsible for calendar ageing: average state of charge during storage ($SOC_{avg,cal}$), average battery temperature (T) and time of storage (t). The operating principle for the cycle ageing evaluation can be summarized as follows:

- SOC time series data (with 1 s sampling rate) elaboration using the Rainflow algorithm
  i. Calculation of cycle depths of discharge (ΔDOD)
  ii. Calculation of average state of charge of the cycles ($SOC_{avg,cyc}$)
  iii. Calculation of time duration of the cycles
  iv. Calculation of full-cycles equivalents cycled during the observation period (FCE)
- Calculation of stress factors using the output parameters of the Rainflow algorithm within the total degradation in reference conditions estimated by proper ageing tests performed by the battery manufacturer.
- Estimation of degradation during the observation period
  i. Estimation of cycle degradation using the cycle degradation model
  ii. Estimation of calendar degradation using the calendar degradation model
  iii. Estimation of total degradation as sum of estimated cycle and calendar degradation

The cycle degradation model is based on Eq. (3) that calculates the cycle degradation for each simulation period ($n\ FCEs$):

$$C_{deg}^{cyc} = \left(F_{deg}^{cyc}(FCE_0) - F_{deg}^{cyc}(FCE_0 + FCE)\right) \cdot S_{\Delta DOD}^{cyc}\left(\Delta DOD, \Delta DOD_{ref}\right) \cdot S_{SOC}^{cyc}\left(SOC, SOC_{ref}\right) \cdot S_T^{cyc}\left(T, T_{ref}\right) \cdot 100\ [\%] \quad (3)$$

The first term is the total cycle degradation in reference conditions $\left(F_{deg}^{cyc}(FCE_0) - F_{deg}^{cyc}(FCE_0 + FCE)\right)$, where F_{deg}^{cyc} is the cycle ageing model for the battery, FCE_0 is the cycle age of the battery at the beginning of the observation period and FCE is the number of full-cycles equivalents elapsed at the observation period. The total cycle degradation of the Samsung SDI NMC cell in reference conditions was obtained from ageing tests performed by the battery manufacturer, and it is used as a reference for the NMC Li-ion cell under investigation [45]. Afterwards, $S_{\Delta DOD}^{cyc}$, S_{SOC}^{cyc} and S_T^{cyc} coefficients determine the effect of each degradation stress factors on cycle degradation. These stress factors coefficients are obtained by the degradation stress factors models $f_{\Delta DOD}^{cyc}$, f_{SOC}^{cyc} and f_{T}^{cyc}. Then, to obtain the degradation in percentage terms, the cycle degradation is multiplied by 100. All the formulations implemented in the cycle degradation model with the corresponding references are listed in Table 1.

Table 1
Degradation stress factor coefficients and models implemented in the cycle-life model.

Cycle ageing degradation model		
Degradation stress factor coefficient	Degradation stress factor model	Reference
$S_{\Delta DOD}^{cyc} = \frac{f_{\Delta DOD}^{cyc}(\Delta DOD_{ref})}{f_{\Delta DOD}^{cyc}(\Delta DOD)}$	$f_{\Delta DOD}^{cyc}(\Delta DOD) = 2.371e^{-2.438\Delta DOD} + 0.7929$	[46] based on data from [47]
$S_{SOC}^{cyc} = \frac{f_{SOC}^{cyc}(SOC_{ref})}{f_{SOC}^{cyc}(SOC)}$	$f_{SOC}^{cyc}(SOC) = \begin{cases} 0.88e^{-\left(\frac{SOC-0.5}{0.3}\right)^2 + 0.12} & 0 \le SOC \le 0.5 \\ 0.745e^{-\left(\frac{SOC-0.5}{0.215}\right)^2 + 0.255} & 0.5 \le SOC \le 1 \end{cases}$	[46] based on data from [48]
$S_T^{cyc} = \frac{f_T^{cyc}(T_{ref})}{f_T^{cyc}(T)}$	$f_{\mathrm{T}}^{cyc}(\mathrm{T}) = e^{-\left(\frac{T-23}{21.5}\right)^2}$	[46] based on data from [47,49,50]

Similarly, the calendar ageing degradation model is based on the following Eq. (4) that calculates the calendar degradation for each simulation time instant ($t = 0, 1, \ldots, t^{tot}$):

$$C_{deg}^{cal} = \left(F_{deg}^{cal}(t_0) - F_{deg}^{cal}(t_0 + t)\right) \cdot S_{SOC}^{cal}\left(SOC, SOC_{ref}\right) \cdot S_T^{cal}\left(T, T_{ref}\right) \cdot 100\ [\%] \quad (4)$$

The first term is the total calendar degradation in reference conditions $\left(F_{deg}^{cal}(t_0) - F_{deg}^{cal}(t_0 + t)\right)$, where F_{deg}^{cal} is the calendar ageing model for the battery, t_0 is the initial calendar age of the battery and t is the length of the time period for which the calendar ageing is estimated. Time t indicate the length of the whole observation period. The total calendar degradation of the specific Samsung SDI NMC cell in reference conditions was obtained from ageing tests performed by the battery manufacturer, and it is used as a reference for the NMC Li-ion cell under investigation [45]. The coefficients S_{SOC}^{cal} and S_T^{cal} estimate the effects of degradation stress factors on calendar degradation. They are based on the degradation stress factor models f_{SOC}^{cal} and f_T^{cal}. Finally, the calendar degradation is multiplied by 100 to obtain the degradation rate in percentage points. All the formulations implemented in the calendar degradation model with the corresponding literature sources are listed

Table 2
Degradation stress factor coefficients and models implemented in the calendar-life model.

Calendar ageing degradation model		
Degradation stress factor coefficient	Degradation stress factor model	Reference
$S_{SOC}^{cal} = \frac{f_{SOC}^{cal}(SOC_{ref})}{f_{SOC}^{cal}(SOC)}$	$f_{SOC}^{cal}(SOC) = 13.7e^{-3.2SOC} + 0.442$	[46] based on data from [48]
$S_T^{cal} = \frac{f_T^{cal}(T_{ref})}{f_T^{cal}(T)}$	$f_{\mathrm{T}}^{cal}(\mathrm{T}) = -0.0264T + 1.6067$	[46] based on data from [49,51]

in Table 2.

At the end, the final output is the total degradation calculated as the sum of estimated cycle ageing degradation and estimated calendar ageing degradation, as expressed by Eq. (5):

$$C_{deg} = C_{deg}^{cyc} + C_{deg}^{cal}\ [\%] \tag{5}$$

These two terms are calculated separated in two different sections of the algorithm: the former allows to evaluate the cycle ageing effect, while the latter calculates the calendar ageing effect. In the cycle ageing section, the degradation is estimated cycle after cycle. Therefore, a "*for cycle*" is used and the degradation is estimated iteratively considering all the micro-cycles countered by the Rainflow algorithm (see Supplementary material). Accordingly, each degradation value is weighted with respect to the depth of discharge of the corresponding cycle. In this way, the estimated cycle ageing degradation (C_{deg}^{cyc}) is evaluated as the sum of all these contributes. Differently, the calendar ageing degradation (C_{deg}^{cal}) is evaluated as a unique value considering the average state of charge and the average temperature over a specific time period. The total degradation (C_{deg}) is the sum of these two components.

As a result, the *SOH* parameter previously defined in Eq. (2) is equal to the difference between the capacity at the beginning of the observation period in percentage terms C_0 and the total degradation evaluated by the degradation model occurring in that observation period C_{deg}, as determined by the following Eq. (6):

$$SOH = C_0 - C_{deg} = C_0 - \left(C_{deg}^{cyc} + C_{deg}^{cal}\right)\ [\%] \tag{6}$$

The *SOH* is equal to 100 % when the battery is new, while it is equal to 80 % when the battery is dead following the EOL criterion. The above-mentioned degradation model significantly depends on the chemistry and type of the battery under investigation. Accordingly, it needs to be modified consistently according to the battery to be modelled.

The results related to the ageing analysis are illustrated in Section 4.1 and in Section 4.2. The above-mentioned degradation model is applied considering different observation periods. Firstly, the ageing model is applied over 3 years of LIBESS operations. In this period the LIBESS performs random cycles according to plant's manager strategy planning and experimental needs without any participation in the energy markets framework. Here, during the first year the capacity at the beginning of the observation period in percentage terms C_0 is considered equal to 100 % (beginning-of-life BOL condition). Differently, during the second and the third year this parameter is equal to the total degradation of the previous year. In this way, the degradation occurred during the first year is the starting point of the second year, and the degradation occurred during the second year is the starting point of the third year. While concerning the power grid services operation, precise weeks have been selected as observation periods. During these weeks, the electrical services described are performed by imposing real power profile commands using automatic power and energy functions. These functions are governed through a local PC-HMI installed in the server room of LIBESS plant and remotely controlled using a specific Web Client application. To make this analysis comparable, the capacity at the beginning of the observation period in percentage terms C_0 is considered equal to 100 % (BOL condition) for all the three services examined.

In summary, the ageing KPIs evaluated are listed as follows:

- the cycle ageing C_{deg}^{cyc} and calendar ageing C_{deg}^{cal} evaluated as battery capacity fade in percentage terms.
- the total ageing capacity fade C_{deg} calculated as the sum of the cycle and calendar ageing.
- the full-cycles equivalents *FCE* performed by the LIBESS during storage operations.
- The relative capacity fade per full-cycles equivalents C_{deg}^{FCE}, hence the amount of capacity loss expressed in [*kWh*] normalized with respect the total number of full-cycles equivalents performed by the battery for the specific storage operation. This last KPI that can be considered as a sort of ageing effect factor is defined by the following Eq. (7):

$$C_{deg}^{FCE} = ((SOH/100)\cdot E_{available})\Big/ FCE\ [kWh/FCE] \tag{7}$$

3.2. Energy performance analysis

The energy analysis is aimed to evaluate the most relevant energy performance indicators of the BESS under investigation. An experimental campaign was conducted aimed at characterizing the system performances from an energetic point of view at different operating conditions. The AC round-trip efficiency and the auxiliaries' mean power were determined at different discharged/charged powers, proportional to the *C-rate*. The goal is to find a dynamic empirical relationship which correlates the AC round-trip efficiency and the auxiliaries' mean power with respect to the AC power exchanged by the battery, using specific fitting functions. We aim to introduce this dynamicity to better account the effect of the working conditions on battery efficiency and life expectancy. The selected fitting functions with their coefficients are defined in the next section in Tables 6 and 7. Moreover, the coefficient of determination (R^2), the sum of squared error (*SSE*) and the 95 % confidence bounds (CB) of the fitted coefficients are evaluated to examine the numerical fit results.

The AC round trip efficiency η_{AC} is defined as the ratio between the useful effect, the discharged energy during the discharge cycle, and the spent effect, the charged energy during the charge cycle, as expressed by Eq. (8):

$$\eta_{AC} = \left(\sum_{dh} P_{AC}\, dt\right)\Big/\left(\sum_{ch} |P_{AC}|\, dt\right) = E_{AC,dh}\Big/ E_{AC,ch}\ [-] \tag{8}$$

The amount of discharged energy in the numerator was obtained by the sum of the AC power P_{AC} exchanged by the battery through the grid interface during the discharge phase second by second. The same calculation was carried out for the charged energy but considering the absolute value due to the sign convention. The AC power data were extrapolated by the supervisory control and data acquisition (SCADA) system with $dt = 1\ [s]$ sampling. For the empirically derived mathematical model, the root extraction of efficiency was used to distinguish between discharge and charge process, by assuming a symmetric efficiency behaviour between discharge and charge. Indeed, a single value of round-trip efficiency was evaluated at different power levels after a complete full cycle. One unit of full cycle denotes one full discharge (from $SOC_{max} = 90\%$ to $SOC_{min} = 10\%$) and one full charge (from $SOC_{min} = 10\%$ to $SOC_{max} = 90\%$). The term *P* is the variable parameter of the model. It is defined in Eq. (9) as the ratio of the AC power exchanged P_{AC} with respect to the nominal power of the LIBESS under investigation P_{nom}.

$$P = P_{AC}/P_{nom} = 0.1 \div 1\ [p.u.] \tag{9}$$

The dynamicity introduced in this empirical model was obtained by varying this term from low power rates to high power rates close to the nominal power. The selected fitting function for the AC round trip efficiency implemented in this work was found in [52]. In this work, C. Betzin et al. [52] demonstrated that the system efficiency strictly depends on the electrical configuration. For this reason, we decided to implement this function because the electrical topology of our LIBESS is similar to that of [52]. More in detail, as depicted in Fig. 3, the electrical scheme of the LIBESS under investigation is composed by two battery banks, two bidirectional inverters (one dedicated to each bank) and one transformer located downstream the inverters.

The same methodology is applied to consider the auxiliaries' mean power behaviour at different power rates. The most common auxiliaries' devices of a LIBESS are related to control and monitoring systems, motorized switches, lightening, SCADA and alarms. But generally, the main contributor to the auxiliaries' energy consumption is the heating

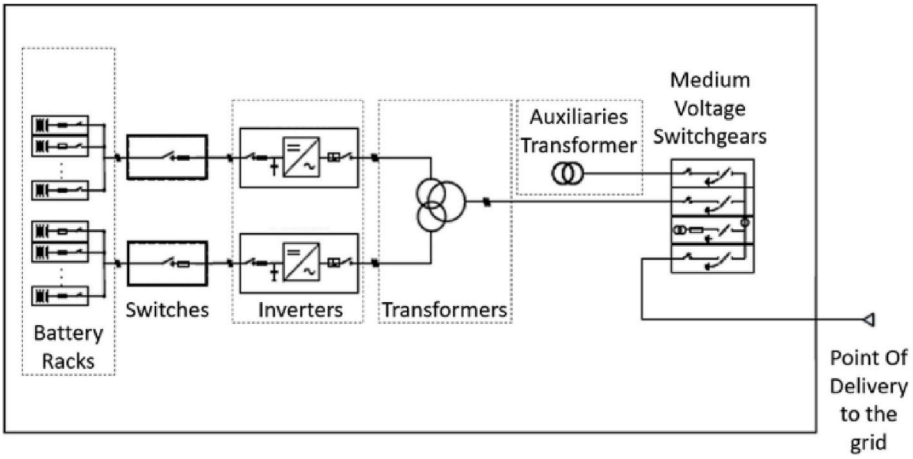

Fig. 3. LIBESS electric topology layout.

ventilation air conditioning system (HVAC) located inside the storage container. In fact, >70 % with respect to the nominal power of the auxiliaries of the LIBESS examined in this work are dedicated to the thermal management system. In this work, the auxiliary dependency is based on the role of thermal conditioning related auxiliaries since they represent the majority of the installed power. This assumption is also made because the data extracted from the SCADA are not available separately for each auxiliaries' unit, but they are measured in a single point. As before, to make this model replicable to other systems with different sizes, it is considered the auxiliaries' mean power normalized, hence the ratio between the auxiliaries' mean power P_{AUX} and the nominal power of the LIBES auxiliary unit $P_{AUX,nom}$, as expressed by Eq. (10):

$$P_{AUX}^{norm} = P_{AUX} / P_{AUX,nom} \; [p.u.] \tag{10}$$

In utility-scale stationary LIBESS industry the use of standard shipping containers to install whole energy storage system devices is the preferred option today. The storage container acts a shield for sensitive electric components from harsh environmental conditions. Moreover, it is filled out with insulation to minimize heat flow from/to the external ambient and maintain a stable operation temperature range to the components inside. The HVAC located inside the storage container is responsible to maintain the Li-ion banks inside a proper temperature range, to ensure safe and optimal operating conditions. In this work, the average cells temperature is maintained between $24.5 \div 26.5 \; [^{\circ}C]$ for most of the time investigated. In Li-ion batteries the heat is mainly due to internal resistance to the passage of current during operations. This kind of batteries are considerably vulnerable to adverse changes in cell temperatures and degrade faster when operated outside of their optimal temperature range [53]. More in detail, this faster degradation may derive from accelerated kinetics for unwanted side reactions occurred at high temperatures, resulting in a loss of capacity and in an increase of the internal resistances [53]. To avoid overheating processes and, in extreme cases, a thermal runaway of the Li-ion cells, it is necessary to extract the heat from the container at a rate greater than the rate of its generation. In this work, the auxiliaries' consumptions have been evaluated at different power rates to obtain a dependency on the AC power exchanged by the battery. Furthermore, other tests in different days and times were executed to detect the seasonal dependency on the ambient temperature.

The energy performance indicators (EPIs) evaluated in this experimental campaign are the global efficiency of operation and the share of losses between battery energy conversion system and auxiliaries. The EPIs are determined according to the following Eqs. (11), (12), (13) and (14):

$$\eta_{global} = \left(\sum_{dh} P_{AC} \, dt\right) \Big/ \left(\sum_{ch} |P_{AC}| \, dt + \sum_{ch} |P_{AUX}| \, dt + \sum_{dh} |P_{AUX}| \, dt\right) = E_{AC,dh} \Big/ \left(E_{AC,ch} + E_{AUX}\right) \; [-] \tag{11}$$

$$L_{global} = 1 - \eta_{global} \; [-] \tag{12}$$

$$L_{BESS} = (1 - \eta_{AC}) / L_{global} \; [-] \tag{13}$$

$$L_{AUX} = (\eta_{AC} - \eta_{global}) / L_{global} \; [-] \tag{14}$$

where P_{AC} is the AC power exchanged by the LIBESS, P_{AUX} is the auxiliaries' power demand, L_{BESS} and L_{AUX} indicates the share of losses due to LIBESS energy conversion and auxiliaries, respectively. As declared for the AC round-trip efficiency definition, the sampling rate is $dt = 1 \; [s]$. It is relevant to remind that all these efficiencies and EPIs were computed considering full cycles, hence the SOC at the beginning is equal to SOC at the end of the test. Therefore, to make these results reciprocally comparable, the basic principle is to consider a time interval during which the initial state of charge is equal to the final state of charge during the selected working cycle.

In this work full discharge and charge cycles were performed exploiting the full range between the minimum ($SOC_{min} = 10\%$) and maximum admissible state of charge level ($SOC_{max} = 90\%$) at different power rates, from low power rates up to consider the LIBESS nominal power. The full discharge/charge cycles are repeated three times for each power rate to verify the consistency of the results obtained. Moreover, these tests are repeated for four different years to investigate the energy performance degradation of the LIBESS. In fact, the results obtained by these several tests present similar value to each other, confirming the validity of the raw data extracted by the SCADA of the BESS under investigation. The experimental campaign is aimed to evaluate the AC round-trip efficiency, the energy performance indicators, and the auxiliaries' mean power at different power rates. An overall description of the experimental activities related to the energy performance analysis is summarized in Table 3. The proposed AC power setpoint are expressed in terms of absolute power (in $[kW]$), in terms of power per unit with respect to the nominal power ($P_{nom} = 500 \; [kW]$), and in terms of *C-rate* with respect to the available capacity ($E_{available} = 657.6 \; [kWh]$). The elapsed time in the last column, expressed in hours, refers to the sum of the discharge cycle duration plus the charge time duration, without considering the idle conditions occurring between the discharge and charge phase.

Table 3
Experimental campaign layout.

Cycle	SOC_{in} [%]	SOC_{fin} [%]	DOD [%]	AC power setpoint [p.u.]	C-rate [C]	Elapsed time [hours]
Cycle @50 kW	10	90	80	0.10	0.08	26.4
Cycle @75 kW	10	90	80	0.15	0.11	17.8
Cycle @100 kW	10	90	80	0.20	0.15	13.2
Cycle @150 kW	10	90	80	0.30	0.23	8.9
Cycle @200 kW	10	90	80	0.40	0.30	6.6
Cycle @250 kW	10	90	80	0.50	0.38	5.3
Cycle @300 kW	10	90	80	0.60	0.46	4.4
Cycle @350 kW	10	90	80	0.70	0.53	3.8
Cycle @400 kW	10	90	80	0.80	0.61	3.3
Cycle @450 kW	10	90	80	0.90	0.68	2.9
Cycle @500 kW	10	90	80	1.00	0.76	2.6

4. Results and discussion

This section presents the results obtained by applying the ageing degradation model and energy performance model via the experimental campaigns described in Methods. Firstly, the results obtained by applying the ageing degradation model were presented considering different observation periods (Sections 4.1 and 4.2). Secondly, the results of the energy performance analysis were discussed separating the results on AC-round trip efficiency (Section 4.3), on auxiliaries' mean power consumption (Section 4.4) and on energy performance indicators (Section 4.5).

4.1. Ageing analysis: LIBESS operations over 3 years

The observation period of LIBESS operating conditions lasts 3 years (Y1, Y2 and Y3) globally and each year is investigated separately. The results of these observation periods are given in Fig. 4(a), (b) and (c), respectively. The top plots show the SOC profile (y-axis) over the observation period expressed in hours (x-axis). As explained in Section 3.1, these time series data extracted by the LIBESS SCADA with a sampling rate of 1 s are elaborated using the Rainflow algorithm. The middle plots represent the total ageing curves, namely the state-of-health (*SOH*) parameter defined in Eq. (6) (y-axis) over the observation period expressed in days (x-axis). The bar plots at the bottom show the total degradation C_{deg}, disaggregated into its components, the cycle ageing C_{deg}^{cyc} and the calendar ageing C_{deg}^{cal}.

The first observation period (a) presents the highest total degradation (1.73%) compared to the other two observation periods (b) and (c) with a total degradation of 1.37% and 1.02%, respectively. It is noteworthy that the total ageing curve represented in the middle plot (a) starts from 100% (BOL condition with a capacity equal to the nominal capacity) and reaches 98.27% after cycling 153 full-cycles equivalents (*FCE*). Then, in the following middle plot (b) the total ageing curve starts from 98.27 % and finishes at 96.9 % after cycling 109 *FCE*. Therefore, the ageing effect of the first year is maintained in the following years. The same for the middle plot (c) that begins at 96.9 % and concludes at 95.88 % performing 93.3 *FCE*. The third observation period (c) exhibits a lower total degradation with respect to the first (a) and the second (b) observation period. This result is in line with the stress factors equations defined in Tables 1 and 2. In fact, as reported in Section 3.1, *SOC* and *ΔDOD* are the most impacting parameters on both cycle and calendar ageing. The *SOC* profile represented in the first year upper plot (a) shows the highest average *SOC* value among all the observation periods ($SOC_{avg,cyc}$ = 52%, see Table 4), deeper *ΔDOD* and rarely ever idle periods with respect to the *SOC* profile in the upper plot (c). The term idle periods refer to those periods characterized by a quasi-steady *SOC* profile and null depth of discharges. The most significant ones occur

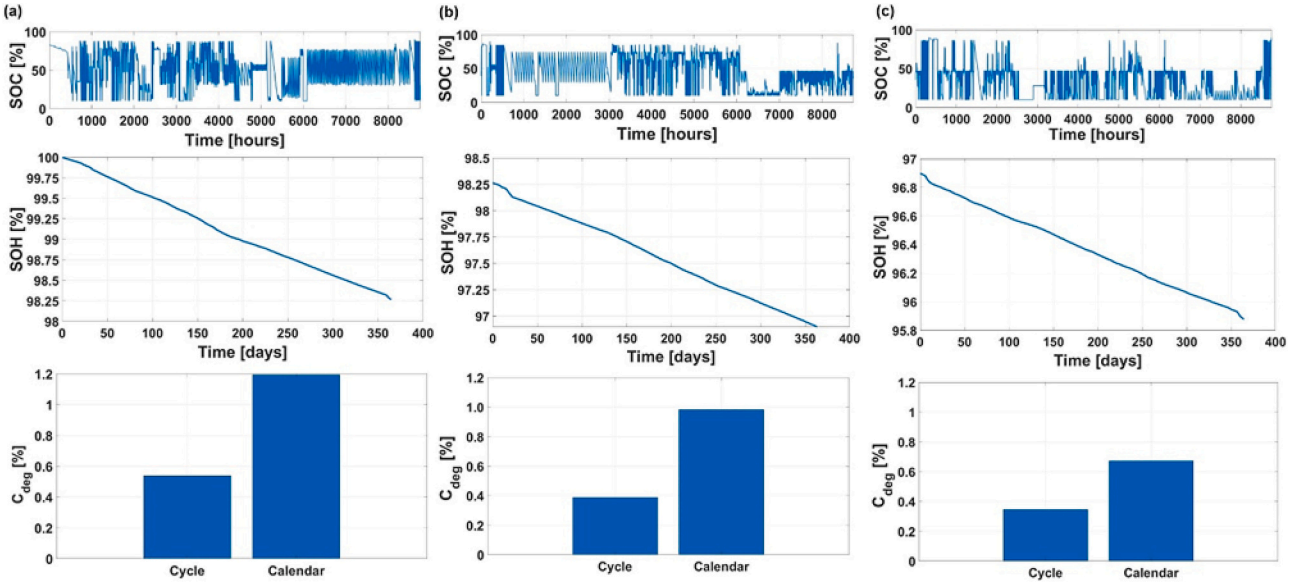

Fig. 4. Ageing degradation model applied on LIBESS normal operations during Y1(a), Y2 (b), and Y3 (c). Top plots: state-of-charge (SOC) profile over the observation period expressed in hours. Middle plots: state-of-health (*SOH*) estimation over the observation period expressed in days. Bottom plots: cycle and calendar capacity fade.

Table 4
Ageing KPIs evaluated by applying the degradation model to LIBESS operations over three years.

Observation period	Elapsed time [days]	Average state of charge $SOC_{avg,cyc}$ [%]	Cycle capacity fade C_{deg}^{cyc} [%]	Full-cycles equivalents FCE [FCE]	Calendar capacity fade C_{deg}^{cal} [%]	Total capacity fade C_{deg} [%]
First year Y1 (a)	365	52.0	0.538	153	1.19	1.73
Second year Y2 (b)	365	45.1	0.388	109	0.983	1.37
Third year Y3 (c)	365	31.8	0.347	94.3	0.673	1.02

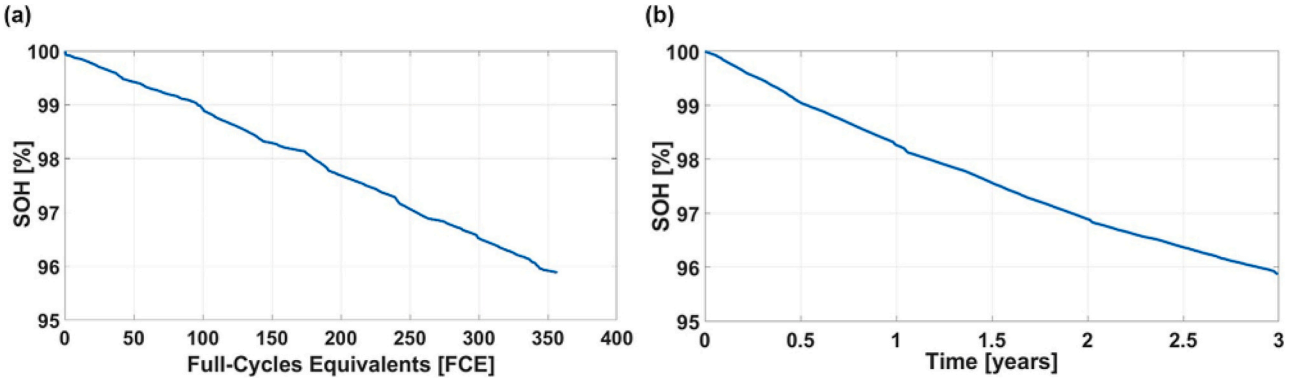

Fig. 5. *SOH* estimated by the dynamic degradation model. *SOH* plotted as a function of the full-cycles equivalents *FCE* (a). *SOH* plotted as a function of the time expressed in years (b).

between $6'000 \div 7'000$ [*hours*] in the second observation period (b), and between $7'000 \div 8'760$ [*hours*] in the third observation period (c). The ageing KPIs for each year are summarized in Table 4.

In summary, considering now the whole investigated period, in Fig. 5 it is represented the state-of-health (*SOH*) calculated by the battery degradation model. In Fig. 5(a) the *SOH* curve is plotted as a function of

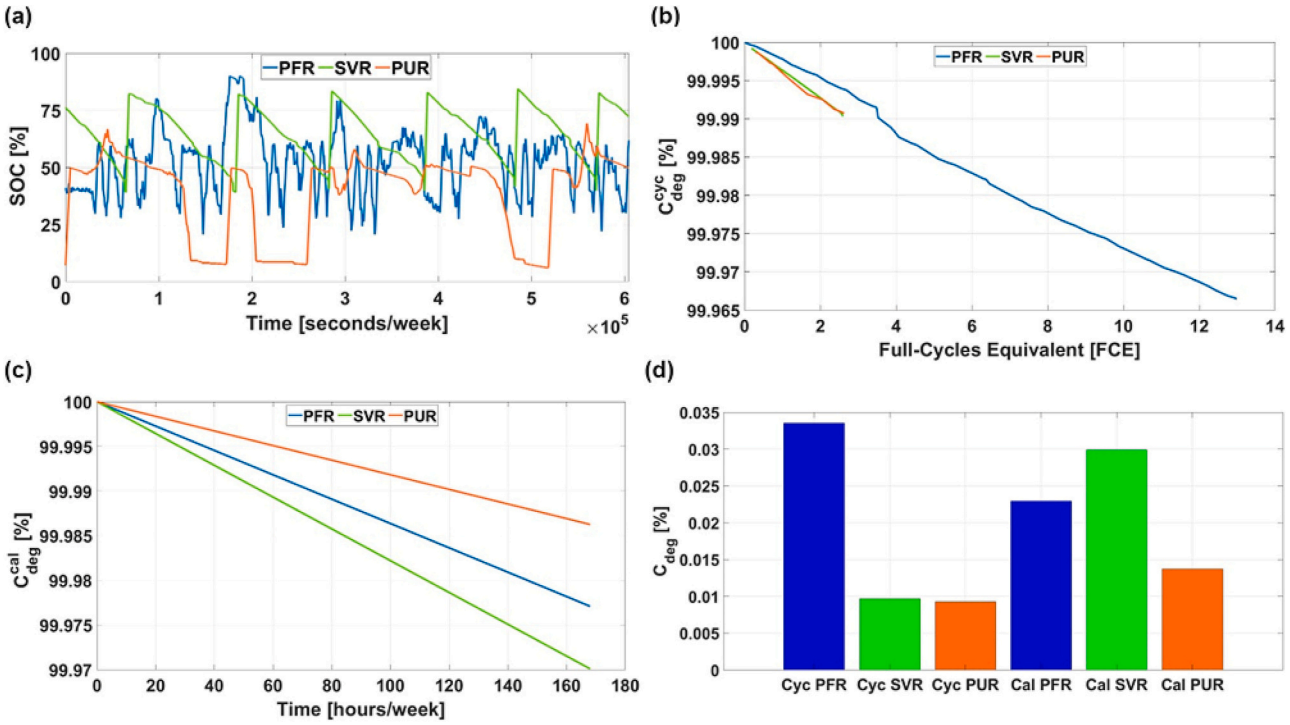

Fig. 6. Ageing degradation model applied on LIBESS power grid services provision. The observation period is 1 week, 168 h, $604'800$ s. The power grid services examined are primary frequency regulation (PFR, blue curve), secondary voltage regulation (SVR, green curve), and PV unbalances reduction (PUR, orange curve). (a) State of charge profile over the observation period expressed in seconds. (b) Capacity fade due to cycle ageing as a function of the full-cycles equivalent. (c) Capacity fade due to calendar ageing over the observation period expressed in hours. (d) Total capacity fade separating the cycle ageing (cyc bars) from the calendar ageing (cal bars). (For interpretation of the references to color in this figure legend, the reader is referred to the web version of this article.)

the *FCE*, while in Fig. 5(b) *SOH* is plotted as a function of the time expressed in years. After about 356 *FCE* and 3 years the *SOH* estimated is equal to 95.88 %. This result is in line with that predicted by the battery manufacturer for the specific Samsung SDI NMC cell, used as a reference for the NMC Li-ion cell under investigation [45]. Typically, battery manufacturers predict a constant degradation rate per FCE, or per year, without considering the effective operations that the battery will perform during its lifetime. This highlights the relevance to introduce a dynamic degradation model that evaluates the *SOH* accordingly to the battery operations because battery manufacturers may not know a priori the actual battery usage.

The battery racks temperature during the LIBESS normal operations is maintained constant and around the reference temperature $T = T_{ref} = 25\ [^{\circ}C]$. Consequently, the battery temperature dependency, expressed by the related temperature stress factors of the ageing model, is not investigated in this section. This assumption is in accordance with the average racks temperature measured inside the container storage system. Indeed, the HVAC system operates properly during the examined observation periods to maintain the battery racks temperature within the desired range, between $24.5 \div 26.5\ [^{\circ}C]$.

4.2. Ageing analysis: LIBESS power grid services provision over 1 week

The results of ageing analysis applied on LIBESS grid services operations are illustrated in Fig. 6. The observation periods are three different weeks during which the LIBESS provides primary frequency regulation (PFR, blue curve), secondary voltage regulation (SVR, green curve), and PV unbalances reduction (PUR, orange curve). Fig. 6(a) compares the SOC profile of the three different power grid applications investigated over one week (604′800 [*seconds*]). Even if the SOC profiles are very irregular, the algorithm is capable to automatically evaluate the number of full-cycles equivalent (FCE) evaluating the depth of discharges, the average state of charge and the end-time of each partial cycle. Fig. 6(b) shows the capacity fade due to cycle ageing in percentage terms (y-axis) as a function of the full-cycles equivalent (FCE) (x-axis) performed by the LIBESS for each grid service examined. Similarly, Fig. 6(c) shows the capacity fade due to calendar ageing (y-axis) over the observation period expressed in hours. Finally, Fig. 6(d) represents the total capacity fade separating the cycle ageing (first three bars) from the calendar ageing (the last three bars) for the three services studied. The KPIs evaluated for each power grid application are summarized in Table 5. To make this analysis comparable, the ageing curves of all electrical services start from 100 % (BOL condition with a capacity of the battery at the beginning of the observation period C_0 equals to 100 %).

At first glance, the data in Fig. 6(d) reveal that PFR seems to be the worst service in terms of total ageing compared to SVR and PUR. Considering only total ageing is not totally exhaustive in the grid services framework. This is because, when a battery performs a power grid service participating in the energy markets, the specific revenue will increase with the amount of discharged/charged energy from/to the grid, hence with the number of full-cycles equivalents that the battery actually runs. Indeed, the full-cycles equivalents cycled during a week are about 13 for PFR and about 3 for SVR and PUR, as we can see from Fig. 6(b) and from the fifth column of Table 5. Moreover, multiplying the total capacity fade normalized with respect to FCE for the available capacity (see Eq. (7)), we obtain one of the most relevant KPIs for the ageing analysis, namely the capacity fade per FCE which is the amount of capacity loss in kilowatt hours per full-cycles equivalent (last column of Table 5). This KPI highlights that PFR is the most efficient service since for each equivalent cycle performed it has a lower ageing loss than SVR and PUR. This consideration will be further demonstrated in the last Section 4.5 by evaluating the energy performance indicators for the selected power grid applications.

Another relevant aspect clearly visible in Fig.6(c) and (d) is that the SVR presents the highest capacity loss due to calendar ageing. The main reason of this behaviour is related to the average SOC value. Observing the SOC profiles displayed in Fig. 6(a), the average SOC value during SVR provision (about 65 [%]) is significantly higher compared to PFR and PUR (about 52 [%] and 39 [%] respectively). On the other hand, PFR emphasizes a remarkably higher capacity loss due to cycle ageing compared to SVR and PUR. This trend is suggested by the steep ups and downs of the SOC profile over time during PFR provision. Consequently, the PFR depth of discharges are more pronounced compared to SVR and PUR that exhibit a more steady and recursive profile.

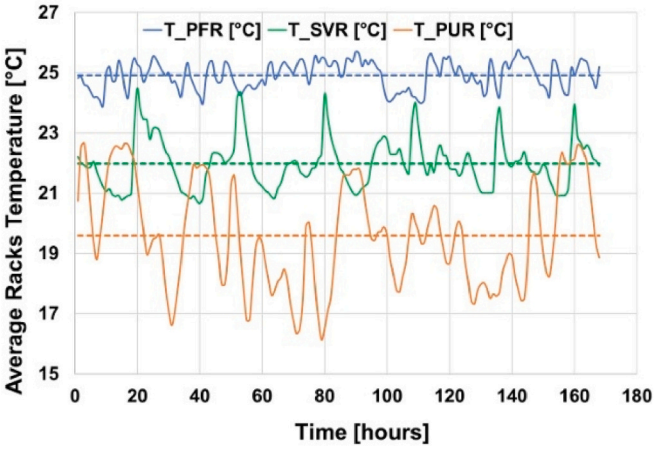

Fig. 7. Average LIBESS Racks Temperature over the observation period for each power grid applications. The observation period is 1 week, 168 h. The power grid services examined are primary frequency regulation (PFR, blue curve), secondary voltage regulation (SVR, green curve), and PV unbalances reduction (PUR, orange curve). The dashed lines are the average values introduced in the ageing degradation model. (For interpretation of the references to color in this figure legend, the reader is referred to the web version of this article.)

Table 5
Ageing KPIs evaluated by applying the degradation model to LIBESS power grid applications provision.

Power grid application	Elapsed time [seconds]	Average LIBESS racks temperature $[^{\circ}C]$	Cycle capacity fade C_{deg}^{cyc} [%]	Full-cycles equivalents *FCE* [FCE]	Calendar capacity fade C_{deg}^{cal} [%]	Total capacity fade C_{deg} [%]	Capacity fade per FCE C_{deg}^{FCE} [kWh/FCE]
Primary frequency regulation (PFR)	604'800	24.9	0.0335	12.987	0.0230	0.0565	0.0286
Secondary voltage regulation (SVR)	604'800	22.0	0.0097	2.603	0.0299	0.0396	0.100
PV unbalances reduction (PUR)	604'800	19.6	0.0093	2.632	0.0137	0.0230	0.0575

The temperature dependency determined by the related temperature stress factors of the ageing model is introduced in this section. The following Fig. 7 plots the average LIBESS racks temperature occurring during the provision of the power grid applications in the selected weeks. These time series data are measured with a sampling rate of 1 h. The dashed lines represent the average values over the observation period that is also reported in Table 5. For primary frequency regulation (PFR) the average value selected is $T_{PFR} = 24.9\,[^{\circ}C]$. For secondary voltage regulation (SVR), the average temperature value is $T_{SVR} = 22.0\,[^{\circ}C]$, while for PV unbalances reduction (PUR) $T_{PUR} = 19.6\,[^{\circ}C]$. These values are introduced in the ageing degradation model, and they correspond to the temperature parameter $T\,[^{\circ}C]$. The temperature effect on cycle and calendar ageing is expressed by the temperature stress factors coefficients defined in Tables 1e and 2, respectively. Nevertheless, it is noteworthy that the temperature dependency on the ageing degradation model has a minor weight compared to the state of charge and depth of discharge dependency. This is because the HVAC system located inside the container storage system is responsible to maintain the LIBESS racks temperature inside a proper range. Therefore, remarkably capacity loss due to sudden racks temperature variations (lower than 15 $[^{\circ}C]$ and higher than 27 $[^{\circ}C]$) were not recorded during the observation periods.

4.3. Energy analysis: AC round-trip efficiency

In this section are illustrated the results obtained following the methodology of the experimental campaign summarized in the previous Table 3. Fig. 8 contains the AC round-trip efficiency curves obtained by fitting the averaged efficiency values evaluated for each power rate. These tests were performed in dedicated periods on a yearly basis over four different years. It is evident that the AC round-trip efficiency curves follow the same trend for all the years examined: low values for low power rates increasing asymptotically towards higher power rates. This behaviour is remarkably consistent with those reported in [18,52]. It is noteworthy that these fitting curves are realized by elaborating real data from a full-scale LIBESS currently in operation and not simulated in laboratory or simulation framework. Moreover, the efficiency curves displayed in Fig. 8 confirm that static battery models based on constant efficiency values are not so accurate: the energy performances of the LIBESS have undergone a decrease, passing from the first year (*dark-blue curve*) to the fourth year (*cyan curve*). Considering the power range between 0.6 and 1 [p.u.], the efficiency decrease is equal to about 4 % with an average value in the flat region of about 93 % for the first year and of 89 % for the fourth year. This trend could be interpreted as a progressive loss over time of cyclable lithium and the consequent growth of the SEI layer at the anode which may trap lithium permanently decreasing in this way the energy performances. This electrochemical degradation mechanism is typically referred to as calendar ageing, namely the battery capacity fade due to degradation of materials composing the battery over time during storage. Another possible explanation of this energy degradation may be due to a progressive increase over time of energy conversion losses (mainly during the charge phase) in the inverter section. The AC round-trip efficiency is generally high with an average value of about 90 %. At low power rates (from 0.1 to 0.3 [p.u.]), the

Table 6
Coefficients a, b, c, their 95 % confidence bounds (CB) and the goodness-of-fit statistics parameters (R^2 and SSE) of the mathematical fitting function for each year examined.

Fitting function	Coefficients (95 % CB)	First year	Second year	Third year	Fourth year
$\eta_{AC}(P) = \frac{a \cdot P}{b+P} + c \cdot P$	a	101.1	97.81	97.30	97.72
	(95 % CB)	(92.5, 109.6)	(71.15, 124.5)	(76.43, 118.2)	(93.17, 102.3)
	b	0.03028	0.02736	0.02692	0.03237
	(95 % CB)	(0.0142, 0.0464)	(−0.0240, 0.0787)	(−0.0134, 0.0673)	(0.0249, 0.0399)
	c	−4.493	−3.065	−3.379	−5.629
	(95 % CB)	(−12.78, 3.793)	(−28.94, 22.81)	(−23.64, 16.88)	(−10.52, −0.7437)
	R^2	0.99948	0.99416	0.99604	0.97301
	(SSE)	(0.02915)	(0.29842)	(0.18479)	(6.6571)

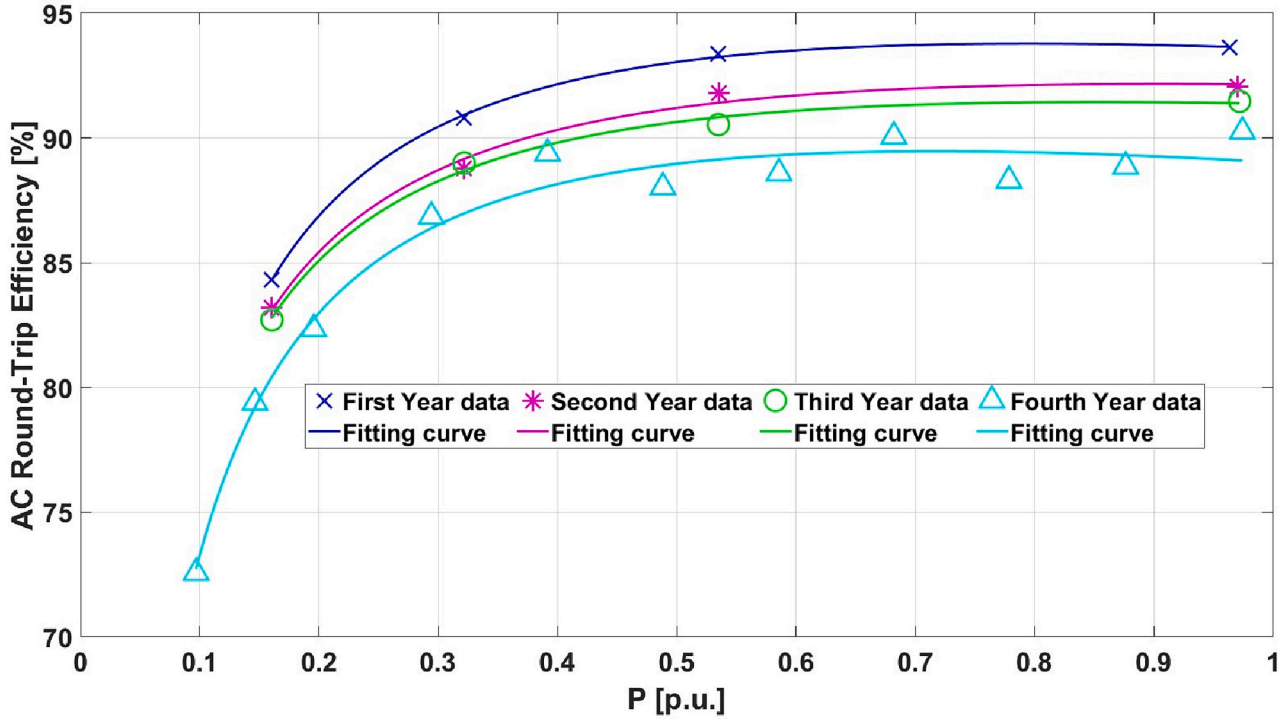

Fig. 8. AC round-trip efficiency curves as a function of the normalized AC power exchanged by the battery P. These curves were elaborated using the specific fitting function defined in the methods section.

power conversion losses prevail, and the AC/AC efficiency decreases considerably. At higher power rates (from 0.5 to 1.0 [p.u.]), the losses mechanisms related to phenomena occurring inside the electrochemical cells prevail, but these phenomena do not significantly affect the AC round-trip efficiency trend. The *a*, *b*, *c* coefficients of the mathematical fitting function implemented are listed in Table 6. Additionally, in Table 6 are reported the R-square (R^2) parameter, the sum of squares due to error (*SSE*), and the 95 % confidence bounds (CB) of the fitted coefficients. The experimental tests carried out in the first three years investigate the efficiency behaviour considering only 4 different power rates ($P = 0.15 - 0.32 - 0.55 - 1$). Differently, the last tests performed in the fourth year includes 11 different power rates with the goal to increase the number of efficiency value in the whole AC power range.

The mathematical fitting function and the correspondent coefficients were evaluated considering the LIBESS under investigation. The system efficiency strictly depends on cell chemistry, internal cell setup and electrical configuration.

4.4. Energy analysis: auxiliaries' mean power

The same methodology of the previous experimental campaign is also applied on the auxiliaries' mean power consumption. In the following Fig. 9, the auxiliaries' mean power consumption values for each different power rates were fitted using a linear function. The y-axis represents the auxiliaries' mean power, while the x-axis indicates the AC power exchanged by the battery normalized always with respect to the nominal power of the LIBESS. Particularly, Fig. 9 shows the auxiliaries' mean power dependency during charges cycles. The dependency during the discharge cycles is not reported due to the very similar behaviour. The orange points and their linear fitting curve correspond to those cycles performed during diurnal hours. The blue points and their linear fitting curve were elaborated considering the discharge/charge cycles performed during night hours. Table 7 presents the coefficients *m* and *q* of the linear fitting function, their 95 % confidence bounds and the goodness-of-fit statistics parameters (R^2 and *SSE*).

The first evident consideration highlighted by this plot is the strong direct proportionality between the AUX mean power and the AC power exchanged by the battery. This is because parts of the auxiliaries' components are directly related to LIBESS operation. Generally, the heating ventilation air conditioning (HVAC) system located inside the storage container is the main contributor to the auxiliaries' energy consumption. The other aspect extrapolated from this plot is that the AUX mean power strongly depends on the ambient conditions: during the diurnal cycles (orange curve) the amount of energy requested by the ventilation system to maintain the set point temperature is higher

Table 7
Coefficients *m*, *q*, their 95 % confidence bounds (CB) and the goodness-of-fit statistics parameters (R^2 and *SSE*) of the linear fitting function.

Fitting function	Coefficients (95 % CB)	Diurnal cycles	Night cycles
$P_{AUX}(P) = m \cdot P + q$	m	0.5125	0.3364
	(95 % CB)	(0.380, 0.645)	(0.276, 0.397)
	q	0.3415	0.2643
	(95 % CB)	(0.265, 0.418)	(0.230, 0.299)
	R^2	0.8943	0.9464
	(SSE)	(0.0274)	(0.00565)

compared to night cycles (blue curve). At lower power rates (from $P = 0.1 \div 0.3$ [*p.u.*]), the delta between diurnal and night cycles of the normalized auxiliary mean power is about $\Delta P_{AUX}^{norm} = 0.1$ [*p.u.*]. This variation increases moving from low to high power rates, reaching a delta of about $\Delta P_{AUX}^{norm} = 0.2$ [*p.u.*] at $P = 0.8 \div 1.0$ [*p.u.*]. The main reason for this behaviour is due to the fact that these tests were carried in the summertime, hence the ambient temperature during the day was higher than that during the night.

As declared before, these coefficients strictly depend on the specific energy storage device investigated (HVAC technologies selected by the LIBESS manufacturer, electrical and thermal dimensioning, LIBESS components internal layout, control strategies). Therefore, the concrete usefulness of this analysis is to provide an experimental set of tests aimed at introducing the concept of dynamism also for the auxiliaries mean power.

Concerning the ambient temperature dependency on AUX mean power, in the following Fig. 10 the AUX mean power normalized, the ambient temperature and the average racks temperature profiles over a typical summer (a) and winter (b) day are compared. As expected, during the central hours of a summer day the auxiliaries' mean power increases rapidly following the trend of the ambient temperature. Therefore, P_{aux} increases with T_{amb} due to the need for the air conditioning of the battery storage container. On the other hand, during a winter day both auxiliaries' mean power and ambient temperature are not subject to sudden variation assuming a constant value throughout the day. Turning now to the AUX mean power dependency on the AC battery power, a similar pattern is set out in Fig. 11 where daily operative conditions (a), and daily idle conditions (b) are compared. In line with the results obtained by the experimental campaign, the auxiliaries' mean power is directly related to battery operative conditions. Indeed, as displayed in Fig. 11(a), the auxiliaries' mean power profile increases and decreases accordingly with the charge/discharge cycles performed by the battery. Differently, during daily idle conditions a base value of

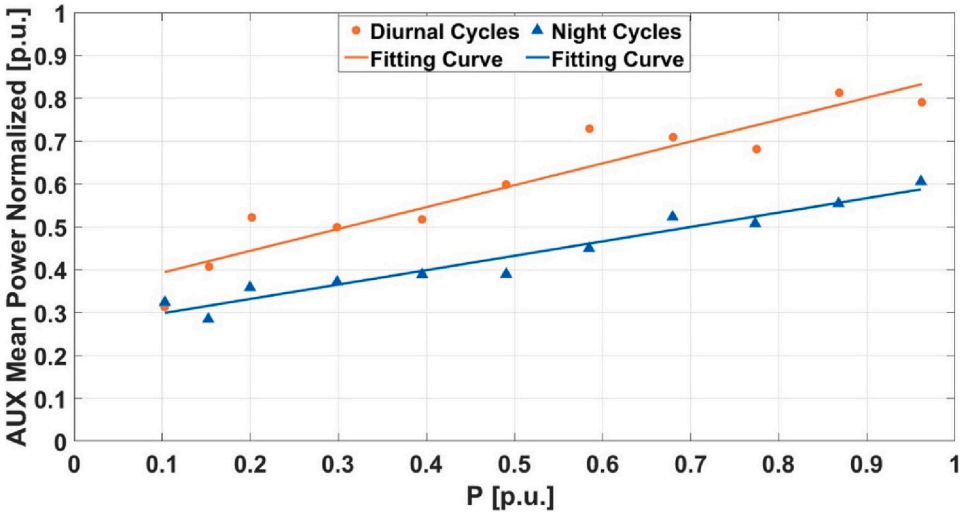

Fig. 9. Auxiliaries mean power normalized with respect to the nominal power of the auxiliary unit as a function of the normalized AC power exchanged by the battery P. The orange points and their linear fitting function indicate the charge cycles performed during diurnal hours. The night points and their linear fitting function indicate the charge cycles performed during night hours. (For interpretation of the references to color in this figure legend, the reader is referred to the web version of this article.)

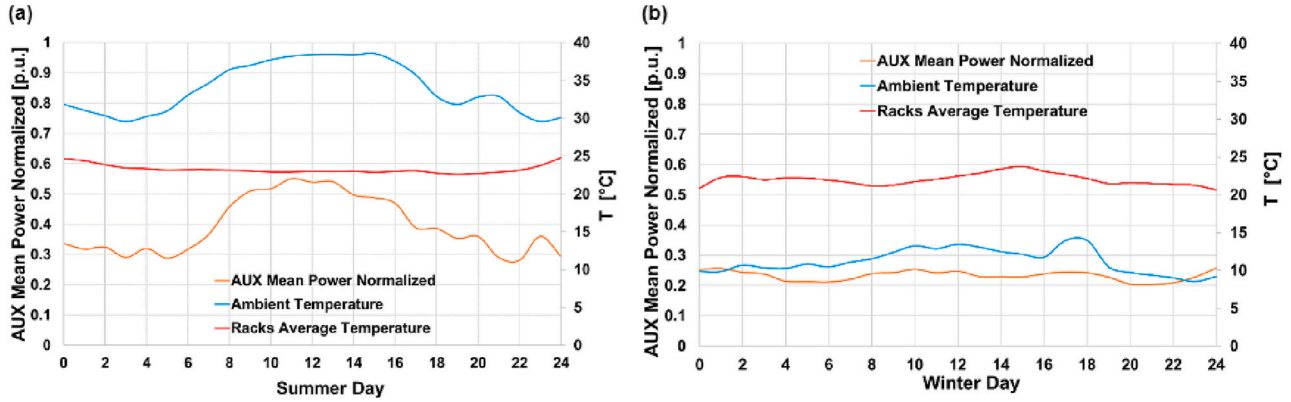

Fig. 10. Auxiliaries' mean power (orange curve), ambient temperature (cyan curve), and average LIBESS racks temperature (red curve) profile over a typical summer day (a) and winter day (b). (For interpretation of the references to color in this figure legend, the reader is referred to the web version of this article.)

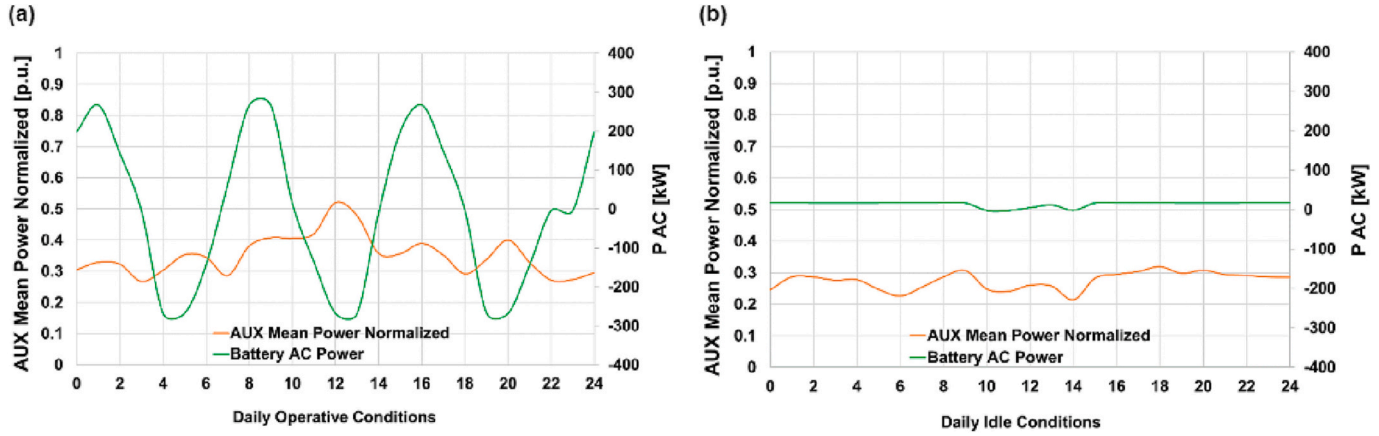

Fig. 11. Auxiliaries' mean power (orange curve) and battery AC power (green curve) profile during daily operative conditions (a) and daily idle conditions (b). (For interpretation of the references to color in this figure legend, the reader is referred to the web version of this article.)

auxiliaries' consumption (about $P_{AUX}^{norm} = 0.25\ [p.u.]$) is always present, supplying those peripheral components that are continuously operating even in idle mode (e.g., SCADA, control and monitoring system, motorized switches, lightening and alarms).

In summary, these results suggest the relevance of detecting the role of auxiliaries' consumption in LIBESS energy performance and lifetime derating. As it for standard modelling techniques, power plant managers cannot be disregarded while modelling the real-world operation of

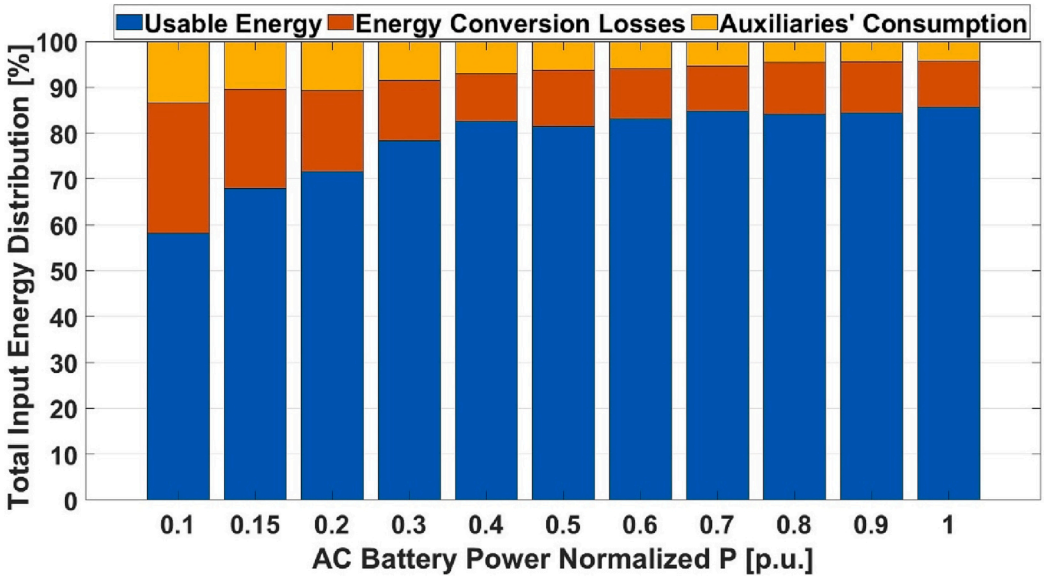

Fig. 12. Total input energy distribution into LIBESS for different power rates.

utility-scale LIBESS facilities, especially in specific business models strongly correlated to LIBESS lifetime.

4.5. Energy analysis: energy performance indicators

In this last section the energy performance indicators (EPIs) are evaluated during LIBESS operations for different power rates and for different power grid applications provision. EPIs are defined in the previous Section 3.2. Fig. 12 presents the total input energy distribution into the system for each power rate examined, separated into usable energy (blue bars), LIBESS energy conversion losses (orange bars), and auxiliaries' consumption (yellow bars). It is evident that LIBESS presents good performances for high power rates close to the nominal power, hence for fast operations with an average global efficiency (blue bars) of about 85 %. Contrarily, for lower power rates and slower operations, the global efficiency decreases to 60–70 % with greater energy conversion losses and auxiliaries' consumption.

In conclusion, in Fig. 13 the EPIs were calculated for the power grid applications investigated in this work: primary frequency regulation (PFR), secondary voltage regulation (SVR), and PV unbalances reduction (PUR). The EPIs of PGAs were obtained considering a specific working cycle provided by LIBESS for the referred application. As for the ageing analysis, PFR is the most efficient service due to higher usable energy partition compared to SVR and PUR. On the contrary, SVR is the worst service in terms of energy performance due to greater energy conversion losses and auxiliaries' consumption losses. Indeed, the global efficiency of PFR is about 83 %, a value considerably higher compared to SVR (about 48 %) and PUR (about 55 %). Energy conversion losses and auxiliaries' consumption are not negligible in all grid services, especially for SVR. These results are in accordance with those obtained by Schimpe et al. [13]. As before, also here it is demonstrated the relevance of including both energy conversion losses and auxiliaries' consumption in battery models, because they account for about 20–40 % of the whole energy input.

5. Conclusions and future work

The current work proposes a data-driven ageing and energy model applied on utility-scale LIBESS currently in operation. The most impacting ageing and energy performance indicators were defined and evaluated considering different observation periods. The experimental protocol implemented to build the developed data-driven model may be easily replicated in any other LIBESS facility equipped with a SCADA with a proper temporal resolution and capable of monitoring the main thermo-electrical physical quantities of the LIBESS plant. Indeed, this experimental procedure based on discharging/charging tests at constant power does not require specific skills in electrochemistry and the ability to test each LIBESS components separately. This could help power plants managers to set a standard experimental procedure to detect the dynamicity of the system efficiency and converting in this way a static battery model into a dynamic battery model. Moreover, this data-driven model might help stakeholders to identify the most impacting key performance indicators (KPIs) on large-scale LIBESS during power grid services provision. The state-of-health (*SOH*) estimated by the degradation model after 3 years and after 356 FCE of LIBESS operations is equal to 95.88 %. During power grid applications, it has been shown that primary frequency regulation is the most efficient service in terms of ageing and energy performance compared to secondary voltage regulation and PV unbalances reduction. A capacity loss of about 0.03 kWh per each full-cycle equivalent has been evaluated during frequency regulation provision. This value is significantly lower compared to secondary voltage regulation (0.1 kWh per each full-cycle equivalent) and to PV unbalances reduction (0.05 kWh per each full-cycle equivalent). During LIBESS operations, the ageing analysis revealed an overall capacity loss, due to cycle and calendar ageing, of about 1.37 % per year with respect to the nominal capacity. The most influencing factors on ageing are SOC range, DOD amplitude, storage time and battery temperature. The energy performance analysis emphasizes the relevance of considering both energy conversion losses and auxiliaries' consumption during normal operating conditions, especially at low power rates during slower operations. The LIBESS presents good performances at high power rates, close to the nominal power with an average global system efficiency of about 85 %. On the contrary, at lower power rates ($P < 0.3\,[p.u.]$), the LIBESS global efficiency decreases to 65 %. Accordingly, possible future novelty research could aim to simulate a hybrid energy storage system (HESS) selecting different ESS

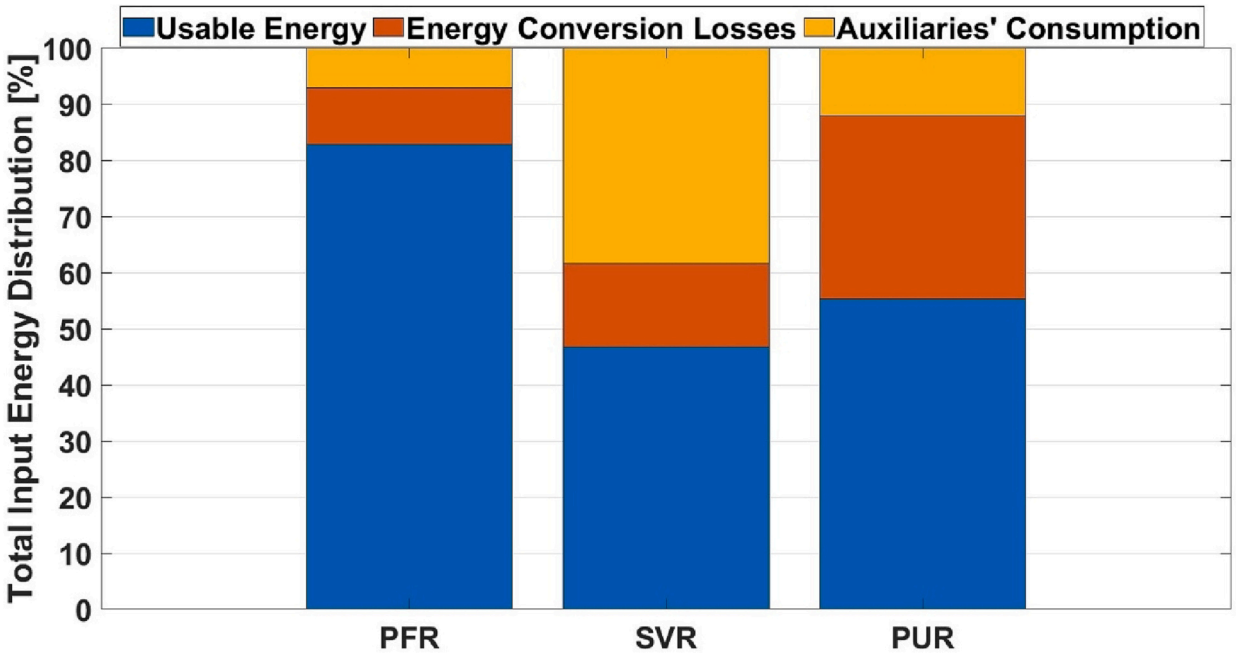

Fig. 13. Total input energy distribution into LIBESS for three different power grid applications: primary frequency regulation (PFR), secondary voltage regulation (SVR), and PV unbalances reduction (PUR).

technologies, tailored to fast and slow market service provision respectively. In this perspective, LIBESS can be suitable for the so-called power-based services that require short-times (time ranges from seconds to minutes), fast provision of the service and high power needed from the infrastructure. On the other hand, a long duration energy storage (LDES) (e.g., redox flow batteries (RFB), solid oxide electrolysers (SOEC), solid oxide fuel cells (SOFC)) can be an efficient solution from a techno-economic point of view for the energy-based services that require longer times (time ranges from hours to days) and slow provision of the service (seasonal storage). In conclusion, this work can be extended to a techno-economic analysis by evaluating the detailed ageing and operating costs during power grid services provision. Therefore, the results obtained from ageing and energy analysis could be combined with the goal to build a business model.

Funding

This research did not receive any specific grant from funding agencies in the public, commercial, or not-for-profit sectors.

CRediT authorship contribution statement

Alberto Grimaldi: Methodology, Software, Investigation, Visualization, Writing – original draft. **Francesco Demetrio Minuto:** Conceptualization, Methodology, Investigation, Writing – review & editing. **Alessandro Perol:** Conceptualization, Methodology, Investigation, Writing – review & editing. **Silvia Casagrande:** Conceptualization, Writing – review & editing. **Andrea Lanzini:** Conceptualization, Methodology, Writing – review & editing, Supervision.

Declaration of competing interest

The authors declare that they have no known competing financial interests or personal relationships that could have appeared to influence the work reported in this paper.

Data availability

The data that has been used is confidential.

Acknowledgement

The authors would like to thank Francesco De Marco, master's degree student at Politecnico di Torino University who helped us with the implementation of the degradation model during his working stage.

Supplementary materials

Supplementary data to this article can be found online at https://doi.org/10.1016/j.est.2023.107232.

References

[1] M.S. Ziegler, J.E. Trancik, Re-examining rates of lithium-ion battery technology improvement and cost decline, EnergyEnviron. Sci. 14 (2021) 1635–1651, https://doi.org/10.1039/d0ee02681f.
[2] L. Mauler, F. Duffner, J. Leker, Economies of scale in battery cell manufacturing: the impact of material and process innovations, Appl. Energy 286 (2021), https://doi.org/10.1016/j.apenergy.2021.116499.
[3] P. Robson, D. Bonomi, D. Research, Growing the battery storage market 2020, n.d, http://www.energystorageforum.com/.
[4] M. Rouholamini, C. Wang, H. Nehrir, X. Hu, Z. Hu, H. Aki, B. Zhao, Z. Miao, K. Strunz, A review of modeling,management, and applications of grid-connected Li-ion battery storage systems, IEEE Trans. Smart Grid 13 (2022) 4505–4524, https://doi.org/10.1109/TSG.2022.3188598.
[5] International Energy Agency, World Energy Outlook 2022, Available from, https://www.iea.org/reports/world-energy-outlook-2022, 2022.
[6] BloombergNEF (BNEF), New Energy Outlook 2020, Executive Summary, Available from, https://about.bnef.com/new-energy-outlook-2020/, 2020.
[7] F. Consortium for Advanced Batteries, National blueprint for lithium batteries executive summary, Available from, https://www.energy.gov/eere/vehicles/articles/national-blueprint-lithium-batteries, 2021.
[8] K. Kessels, B. Mantels, C. Hussy, M. Bons, F. Comaty, M. Goes, F. Wiersma, A. Kshemendranat, C. Christensen, P. Hochloff, D. Schledde, European Commission-N° ENER C2/2015-410 Support to R&D strategy for battery based energy storage Costs and benefits for deployment scenarios of battery systems (D7)-Support to R&D Strategy for battery based energy storage Costs and benefits for deployment scenarios of battery systems (D7), 2016.
[9] P. Office of the European Union, Clean energy for all Europeans Energy, Available from, https://energy.ec.europa.eu/topics/energy-strategy/clean-energy-all-europeans-package_en.
[10] European Commission, The European Green Deal, Brussels, COM (2019) 640 final, Available from, https://ec.europa.eu/info/sites/default/files/european-green-deal-communication_en.pdf.
[11] A.v. Vykhodtsev, D. Jang, Q. Wang, W. Rosehart, H. Zareipour, A review of modelling approaches to characterize lithium-ion battery energy storage systems in techno-economic analyses of power systems, Renew. Sustain. Energy Rev. 166 (2022), 112584, https://doi.org/10.1016/j.rser.2022.112584.
[12] A. Jokar, B. Rajabloo, M. Désilets, M. Lacroix, Review of simplified pseudo-two-dimensional models of lithium-ion batteries, J. Power Sources 327 (2016) 44–55, https://doi.org/10.1016/j.jpowsour.2016.07.036.
[13] M. Schimpe, M. Naumann, N. Truong, H.C. Hesse, S. Santhanagopalan, A. Saxon, A. Jossen, Energy efficiency evaluation of a stationary lithium-ion battery container storage system via electro-thermal modeling and detailed component analysis, Appl. Energy 210 (2018) 211–229, https://doi.org/10.1016/j.apenergy.2017.10.129.
[14] F.M. Gatta, A. Geri, S. Lauria, M. Maccioni, F. Palone, Battery energy storage efficiency calculation including auxiliary losses: technology comparison and operating strategies, in: 2015 IEEE Eindhoven PowerTech, PowerTech 2015, Institute of Electrical and Electronics Engineers Inc., 2015, https://doi.org/10.1109/PTC.2015.7232464.
[15] P. Keil, S.F. Schuster, J. Wilhelm, J. Travi, A. Hauser, R.C. Karl, A. Jossen, Calendar aging of lithium-ion batteries, J. Electrochem. Soc. 163 (2016) A1872–A1880, https://doi.org/10.1149/2.0411609jes.
[16] C. Brivio, V. Musolino, M. Merlo, C. Ballif, A physically-based electrical model for lithium-ion cells, IEEE Trans.Energy Convers. 34 (2019) 594–603, https://doi.org/10.1109/TEC.2018.2869272.
[17] C. Brivio, V. Musolino, P.J. Alet, M. Merlo, A. Hutter, C. Ballif, Application-independent protocol for predicting the efficiency of lithium-ion battery cells in operations, J. Energy Storage 15 (2018) 415–422, https://doi.org/10.1016/j.est.2017.11.021.
[18] G. Rancilio, A. Lucas, E. Kotsakis, G. Fulli, M. Merlo, M. Delfanti, M. Masera, Modeling a large-scale battery energy storage system for power grid application analysis, Energies 12 (2019), https://doi.org/10.3390/en12173312. Basel.
[19] D. Choi, N. Shamim, A. Crawford, Q. Huang, C.K. Vartanian, V.v. Viswanathan, M. D. Paiss, M.J.E. Alam, D.M. Reed, V.L. Sprenkle, Li-ion battery technology for grid application, J. Power Sources 511 (2021), https://doi.org/10.1016/j.jpowsour.2021.230419.
[20] B. Xu, Y. Shi, D.S. Kirschen, B. Zhang, Optimal battery participation in frequency regulation markets, IEEE Trans. Power Syst. 33 (2018) 6715–6725, https://doi.org/10.1109/TPWRS.2018.2846774.
[21] F. Sorourifar, V.M. Zavala, A.W. Dowling, Integrated multiscale design, market participation, and replacement strategies for battery energy storage systems, IEEE Trans. Sustain.Energy 11 (2020) 84–92, https://doi.org/10.1109/TSTE.2018.2884317.
[22] M. Matshuishi, T. Endo, Fatigue of metals subjected to varying stress, in: Proceedings of Japan Society of Mechanical Engineering, Fukuoka, Japan, 1968.
[23] N. Diorio, A. Dobos, S. Janzou, A. Nelson, B. Lundstrom, Technoeconomic modeling of battery energy storage in SAM, 2015 www.nrel.gov/publications.
[24] M. Chawla, R. Naik, R. Burra, H. Wiegman, Utility energy storage life degradation estimation method, Available from, in: 2010 IEEE Conference on Innovative Technologies for an Efficient and Reliable Electricity Supply, CITRES 2010, 2010, pp. 302–308, https://doi.org/10.1109/CITRES.2010.5619790.
[25] H. Rauf, M. Khalid, N. Arshad, Machine learning in state of health and remaining useful life estimation: theoretical and technological development in battery degradation modelling, Renew. Sust. Energ. Rev. 156 (2022), https://doi.org/10.1016/j.rser.2021.111903.
[26] G. He, Q. Chen, C. Kang, P. Pinson, Q. Xia, Optimal bidding strategy of battery storage in power markets considering performance-based regulation and battery cycle life, IEEE Trans. Smart Grid. 7 (2016) 2359–2367, https://doi.org/10.1109/TSG.2015.2424314.
[27] N. Padmanabhan, M. Ahmed, K. Bhattacharya, Battery energy storage systems in energy and reserve markets, IEEE Trans. Power Syst. 35 (2020) 215–226, https://doi.org/10.1109/TPWRS.2019.2936131.
[28] H.C. Hesse, V. Kumtepeli, M. Schimpe, J. Reniers, D.A. Howey, A. Tripathi, Y. Wang, A. Jossen, Ageing and efficiency aware battery dispatch for arbitrage markets using mixed integer linear programming, Energies 12 (2019), https://doi.org/10.3390/en12060999. Basel.
[29] K. Moy, S.B. Lee, S. Harris, S. Onori, Design and validation of synthetic duty cycles for grid energy storage dispatch using lithium-ion batteries, Adv.Appl.Energy 4 (2021), https://doi.org/10.1016/j.adapen.2021.100065.
[30] S. Karagiannopoulos, A. Rigas, N. Hatziargyriou, G. Hug, A. Oudalov, Battery energy storage capacity fading and control strategies for deterministic and stochastic power profiles, in: 19th Power Systems Computation Conference, PSCC

2016, Institute of Electrical and Electronics Engineers Inc., 2016, https://doi.org/10.1109/PSCC.2016.7540956.
[31] I. Bloom B.W. Cole J.J. Sohn S.A. Jones E.G. Polzin V.S. Battaglia G.L. Henriksen C. Motloch R. Richardson T. Unkelhaeuser D. Ingersoll H.L. Case , An accelerated calendar and cycle life study of Li-ion cells, n.d.
[32] E. Sarasketa-Zabala, E. Martinez-Laserna, M. Berecibar, I. Gandiaga, L. M. Rodriguez-Martinez, I. Villarreal, Realistic lifetime prediction approach for Li-ion batteries, Appl. Energy 162 (2016) 839–852, https://doi.org/10.1016/j.apenergy.2015.10.115.
[33] M. Schimpe, M.E. von Kuepach, M. Naumann, H.C. Hesse, K. Smith, A. Jossen, Comprehensive modeling of temperature-dependent degradation mechanisms in lithium iron phosphate batteries, J. Electrochem. Soc. 165 (2018) A181–A193, https://doi.org/10.1149/2.1181714jes.
[34] T. Raj, A.A. Wang, C.W. Monroe, D.A. Howey, Investigation of path-dependent degradation in lithium-ion batteries**, 2020, https://doi.org/10.5287/bodleian:v0ervBv6p.
[35] L. Zhou, S. Pan, J. Wang, A.V. Vasilakos, Machine learning on big data: opportunities and challenges, Neurocomputing 237 (2017) 350–361, https://doi.org/10.1016/j.neucom.2017.01.026.
[36] Y. Yang, Q. Zhou, L. Zhang, D. Du, M. Zheng, Q. Niu, L. Gao, X. Yuan, Recent progresses in state estimation of lithium-ion battery energy storage systems: a review, Trans. Inst. Meas. Control. (2022), https://doi.org/10.1177/01423312221124354.
[37] M. Lucu, E. Martinez-Laserna, I. Gandiaga, K. Liu, H. Camblong, W.D. Widanage, J. Marco, Data-driven nonparametric Li-ion battery ageing model aiming at learning from real operation data - part B: cycling operation, J. Energy Storage 30 (2020), https://doi.org/10.1016/j.est.2020.101410.
[38] Y. Li, J. Chen, F. Lan, Enhanced online model identification and state of charge estimation for lithium-ion battery under noise corrupted measurements by bias compensation recursive least squares, J. Power Sources 456 (2020), https://doi.org/10.1016/j.jpowsour.2020.227984.
[39] Z. Wei, S. Meng, B. Xiong, D. Ji, K.J. Tseng, Enhanced online model identification and state of charge estimation for lithium-ion battery with a FBCRLS based observer, Appl. Energy 181 (2016) 332–341, https://doi.org/10.1016/j.apenergy.2016.08.103.
[40] Y. Cui, C. Du, G. Yin, Y. Gao, L. Zhang, T. Guan, L. Yang, F. Wang, Multi-stress factor model for cycle lifetime prediction of lithium ion batteries with shallow-depth discharge, J. Power Sources 279 (2015) 123–132, https://doi.org/10.1016/j.jpowsour.2015.01.003.
[41] J.S. Edge, S. O'Kane, R. Prosser, N.D. Kirkaldy, A.N. Patel, A. Hales, A. Ghosh, W. Ai, J. Chen, J. Yang, S. Li, M.C. Pang, L. Bravo Diaz, A. Tomaszewska, M. W. Marzook, K.N. Radhakrishnan, H. Wang, Y. Patel, B. Wu, G.J. Offer, Lithium ion battery degradation: what you need to know, Phys. Chem. Chem. Phys. 23 (2021) 8200–8221, https://doi.org/10.1039/d1cp00359c.
[42] M.S. Hosen, D. Karimi, T. Kalogiannis, A. Pirooz, J. Jaguemont, M. Berecibar, J. Van Mierlo, Electro-aging model development of nickel-manganese-cobalt lithium-ion technology validated with light and heavy-duty real-life profiles, J. Energy Storage 28 (2020), https://doi.org/10.1016/j.est.2020.101265.
[43] I. Baghdadi, O. Briat, J.Y. Delétage, P. Gyan, J.M. Vinassa, Lithium battery aging model based on Dakin's degradation approach, J. Power Sources 325 (2016) 273–285, https://doi.org/10.1016/j.jpowsour.2016.06.036.
[44] N. Collath, B. Tepe, S. Englberger, A. Jossen, H. Hesse, Aging aware operation of lithium-ion battery energy storage systems: a review, J. Energy Storage 55 (2022). 10.14459/2022m.
[45] Smart battery systems for energy storage, Samsung_SDI_94Ah_Datasheet, Available from, https://www.samsungsdi.com/upload/ess_brochure/Samsung%20SDI%20brochure_EN.pdf.
[46] S. Jenu, S. Tuurala, A. Manninen, M. Myllysilta, I. Deviatkin, K. Koponen, A. Hentunen, Advanced state of health diagnostics tool, INVADE, H2020 project, Grant agreement n° 731148, Available from, https://h2020invade.eu/wp-content/uploads/2017/05/D6.4-Advanced-state-of-health-diagnostics-tool.pdf.
[47] J. Wang, J. Purewal, P. Liu, J. Hicks-Garner, S. Soukazian, E. Sherman, A. Sorenson, L. Vu, H. Tataria, M.W. Verbrugge, Degradation of lithium ion batteries employing graphite negatives and nickel-cobalt-manganese oxide + spinel manganese oxide positives: part 1, aging mechanisms and life estimation, J. Power Sources 269 (2014) 937–948, https://doi.org/10.1016/j.jpowsour.2014.07.030.
[48] M. Ecker, N. Nieto, S. Käbitz, J. Schmalstieg, H. Blanke, A. Warnecke, D.U. Sauer, Calendar and cycle life study of Li(NiMnCo)O2-based 18650 lithium-ion batteries, J. Power Sources 248 (2014) 839–851, https://doi.org/10.1016/j.jpowsour.2013.09.143.
[49] F. Richter, P.J.S. Vie, S. Kjelstrup, O.S. Burheim, Measurements of ageing and thermal conductivity in a secondary NMC-hard carbon Li-ion battery and the impact on internal temperature profiles, Electrochim. Acta 250 (2017) 228–237, https://doi.org/10.1016/j.electacta.2017.07.173.
[50] S. Käbitz, J.B. Gerschler, M. Ecker, Y. Yurdagel, B. Emmermacher, D. André, T. Mitsch, D.U. Sauer, Cycle and calendar life study of a graphite|LiNi1/3Mn 1/3Co1/3O2 Li-ion high energy system.Part A: full cell characterization, J. Power Sources 239 (2013) 572–583, https://doi.org/10.1016/j.jpowsour.2013.03.045.
[51] J. Schmitt, A. Maheshwari, M. Heck, S. Lux, M. Vetter, Impedance change and capacity fade of lithium nickel manganese cobalt oxide-based batteries during calendar aging, J. Power Sources 353 (2017) 183–194, https://doi.org/10.1016/j.jpowsour.2017.03.090.
[52] C. Betzin, H. Wolfschmidt, M. Luther, Electrical operation behavior and energy efficiency of battery systems in a virtual storage power plant for primary control reserve, Int.J.Electr.PowerEnergy Syst. 97 (2018) 138–145, https://doi.org/10.1016/j.ijepes.2017.10.038.
[53] S. Ma, M. Jiang, P. Tao, C. Song, J. Wu, J. Wang, T. Deng, W. Shang, Temperature effect and thermal impact in lithium-ion batteries: a review, Prog.Nat.Sci.Mater. Int. 28 (2018) 653–666, https://doi.org/10.1016/j.pnsc.2018.11.002.